The Depositional Record
The journal of the International Association of Sedimentologists
Open Access

ORIGINAL RESEARCH ARTICLE

Microbial sedimentary imprint on the deep Dead Sea sediment

CAMILLE THOMAS*,[1], YAEL EBERT†, YAEL KIRO‡, MORDECHAI STEIN§, DANIEL ARIZTEGUI* and THE DSDDP SCIENTIFIC TEAM

*Department of Earth Sciences, University of Geneva, rue des Maraichers 13, Geneva CH 1205, Switzerland (E-mail: camille.thomas@univ-savoie.fr)
†Institute of Earth Sciences, Hebrew University of Jerusalem, Edmond J. Safra Campus, Givat Ram, Jerusalem, IL 91904, USA
‡Lamont-Doherty Earth Observatory, Columbia University, 61 Rt. 9W, Palisades, NY 10964, USA
§Geological Survey of Israel, 30 Malkhe Israel St., Jerusalem, IL 95501, USA

Keywords
EPS, geomicrobiology, hypersaline, iron-sulphur mineralization.

[1]Present address: UMR 42 CARRTEL, Alpine Research Center on Lake Food Webs, University of Savoie Mont-Blanc, 73376 Le Bourget du Lac, France

Manuscript received: 24 September 2015; Accepted: 28 April 2016

doi: 10.1002/dep2.16

ABSTRACT

A study of an International Continental Drilling Program core recovered from the middle of the modern Dead Sea has identified microbial traces within this subsurface hypersaline environment. A comparison with an active microbial mat exhibiting similar evaporative processes characterized iron-sulphur mineralization and exopolymeric substances resulting from microbial activity. Exopolymeric substances were identified in the drilled sediment but unlike other hypersaline environments, it appears that they have a limited effect on the precipitation of calcium carbonate in the sedimentary column. Sulphate reduction, however, plays a role in all types of evaporative facies, leading to the formation of diagenetic iron sulphides in glacial and interglacial intervals. Their synthesis seems to occur under progressive sulphidation that generally stops at greigite because of incomplete sulphate reduction. The latter may be caused by a lack of suitable organic matter in this hypersaline, hence energy-demanding, environment. Pyrite may be found in periods of high lake productivity, when more labile organic matter is available. The carbon and sulphur cycles are thus influenced by microbial activity in the Dead Sea environment and this influence results in diagenetic transformations in the deep sediment.

INTRODUCTION

The Dead Sea is one of the most saline lakes in the world. In addition, it also has extremely high levels of divalent cations Ca^{2+} and Mg^{2+}, making it even harder for life to cope with its chemistry (Nissenbaum, 1975). While few microbes have adapted to such environments, successful colonists include *Archaea* members of the extreme halophilic class *Halobacteria*, as well as a few halophilic *Bacteria* (Bodaker *et al.*, 2010; Rhodes *et al.*, 2012).

In such an environment, salinity gradients encourage and support life. Submarine freshwater springs host numerous and diverse microbial mats benefiting from local dilution of the brine (Ionescu *et al.*, 2012). In the recent past, rainy winters have also brought enough freshwater to the lake to dilute the shallow layers by 70%, enabling blooms of the halophilic algae *Dunaliella parva* (Oren & Shilo, 1982; Oren *et al.*, 1995). The highly labile organic matter produced by the autotrophic eukaryotes would have been immediately degraded by blooms of *Halobacteria* (Oren, 1983).

The microbial influence on the Dead Sea subsurface is less well-known. The recovery of a 457 m long core from the deepest part of the lake via the International Continental Drilling Program (ICDP)-funded Dead Sea Deep Drilling Project (DSDDP) has shown a potential for climatic and palaeoenvironmental reconstructions (Lazar *et al.*, 2014; Neugebauer *et al.*, 2014; Torfstein *et al.*, 2015). In order to constrain the impact of microbial activity on this pristine archive, a geomicrobiological investigation was performed. Initial results revealed the importance of assessing the role of microbial activity in the early diagenesis of the Dead Sea sediment, highlighting differential distribution of microbes with diverse functional potential along the core (Thomas *et al.*, 2014; Ariztegui *et al.*, 2015). The DSDDP project also provides a unique opportunity to explore the diagenetic processes

occurring in the sediment of the Dead Sea before they become exposed and fully desiccated.

Here, we investigate the potential traces of past or current microbial activity in the Dead Sea depositional record, and qualify early diagenesis in its deep sediment. In order to do so, the sedimentology and mineralogy of an active microbial mat from the western shore of the Dead Sea have been examined and identified microbial traces were searched for in the cored material.

Hypersaline environments often allow for the growth of microbial mats as their salinity prevents the development of grazing communities (Des Marais, 1995). Being often close to saturation with respect to halite, gypsum and calcium carbonates, it can be difficult to differentiate abiotic mineralization from organomineralization. The role of EPS as a matrix for mineral nucleation, particle binding or cation concentration is a cornerstone of the calcium carbonate mineralization in hypersaline sediments (Dupraz *et al.*, 2004; Dupraz & Visscher, 2005). We address EPS recognition and its role in the Dead Sea realm, which is known to precipitate aragonite abiotically from the lake water column (Stein *et al.*, 1997). In addition, the iron-sulphur mineralization previously recognized as diagenetic phases in palaeomagnetic studies (Ron *et al.*, 2006) is further investigated. Studies of the subsurface waters of the Dead Sea Basin have highlighted major redox transformations affecting carbon, iron and sulphur among other elements (Avrahamov *et al.*, 2010, 2014; Kiro *et al.*, 2013). It is therefore necessary to assess the extent of such changes and whether they reach the deepest region of the Dead Sea Basin, or if they are constrained to the aquifer/brine interface at its shoulders.

GEOLOGICAL AND LIMNOLOGICAL SETTING

The Dead Sea is located on the lowest spot on continental Earth, at a current elevation of 428·9 m b.s.l (2015). Today's water salinity is among the highest on Earth for a lake of this size, reaching 348 g L^{-1} of total dissolved salts (Oren & Gunde-Cimerman, 2012). Intensive use of catchment area water for irrigation, and potash mining have led to a decrease in water level over the last 40 years at an average rate of 0·7 m per year (Abu Ghazleh *et al.*, 2009; Tahal Group and the Geological Survey of Israel, 2011). Rare freshwater inputs bringing nutrients and carbonate ions to the lake are the Jordan River, and in rainy periods, flash floods fed by canyons (wadis) cutting through the Judean Mountains and the Jordanian Plateaus.

Before 1979, sufficiently rainy conditions had allowed a diluted epilimnion to establish through the mixing of freshwater with the calcium-chlorine brine of the Dead Sea. Anoxic conditions developed in the resulting hypolimnion, leading to high hydrogen sulphide concentration and the occurrence of iron sulphide explained by bacterial sulphate reduction activity (Nissenbaum, 1975; Nishri & Stiller, 1984). These conditions disappeared quickly from the water column after complete overturn in the winter of 1978–1979 (Steinhorn *et al.*, 1979). Exceptionally rainy winters in 1980 and 1991 led to the renewed formation of temporal meromictic conditions. The diluted epilimnion constituted a less extreme environment in which the halophilic Green Algae *Dunaliella* could develop and bloom, imparting a red colour to the lake (Oren & Shilo, 1982; Oren *et al.*, 1995).

An array of evidence suggests the presence of relatively similar conditions supporting the influence of life on the geochemical record of the Lake Lisan sediment. For example, within the Lisan Formation in the Perazim Valley (west of the Dead Sea southern basin), a general increase in the $\delta^{13}C$ of the aragonite laminae deposited during the last glacial period has been interpreted as a result of increasing autotrophic activity in the palaeo-epilimnion (Kolodny *et al.*, 2005).

Sulphur isotopes from gypsum intervals also support the occurrence of active sulphate reduction in the water column and bottom sediment of the lake (Torfstein *et al.*, 2005, 2008). Negative $\delta^{34}S$ values from disseminated gypsum and thin gypsum laminae of the Lisan Formation (from $-26‰$ to $1‰$) are interpreted as being a result of bacterial sulphate reduction in the anoxic hypersaline palaeo-hypolimnion. Sulphur concretions from the Masada section also bear lighter $\delta^{34}S$ isotopes than the surrounding gypsum values (27 to 29 ‰ lower) and iron and manganese concentration gradients were interpreted to result from incomplete microbial sulphate reduction terminating at S^0 (Bishop *et al.*, 2013).

The two limnological regimes of the lake are reflected in the nature of the evaporitic minerals precipitating in both situations, constituting a good proxy for changes in the limnological regime. During meromictic conditions, aragonite precipitation dominates (Stein *et al.*, 1997). This is emphasized in outcrops and core material by alternating laminae of aragonite and detrital marls (AAD), indicative of glacial periods (Stein *et al.*, 1997; Neugebauer *et al.*, 2014). During periods of increasing aridity, the lake becomes holomictic and gypsum precipitation occurs, followed by halite deposition. This type of deposit, intercalated by detrital sediment is largely dominant in interglacial periods. Since carbon and sulphur cycles vary greatly from one situation to another, our analyses are linked to these different types of facies in order to tackle the microbial impact on the Dead Sea sediment.

MATERIAL

A microbial mat was collected from an ephemeral saline pond on the western shore of the Dead Sea, near the En Qedem spring site (Fig. 1B). Salinity of the pond has reached 36·9%, with concentrations of major elements as follows: Na^+ = 2·12 M, Ca^{2+} = 0·58 M, Mg^{2+} = 1·59 M and Cl^- = 6·11 M and SO_4^{2-} = 18·9 mM, slightly above those of the current Dead Sea water (Ionescu *et al.*, 2012). The upper part of the mat consists of a gypsum and halite-rich biofilm (Fig. 1E) coloured by red pigments originating mainly from the carotenoids of *Dunaliella* cells, which have developed in the diluted water of the ephemeral pond (Fig. 1D). Microbial communities were analysed (Thomas *et al.*, 2015) and are mainly composed of heterotrophic *Archaea* of the *Halobacteria* class, while almost no bacterial DNA could be sequenced. Aragonite stellate clusters are also present in the mat as a result of aragonite needles precipitating from the pond water (Fig. 2A). Below this EPS-rich red layer (Fig. 2B and C), alternating laminae of pure aragonite (white), mixed aragonite and detrital material (light grey), and detrital sediment only (dark grey) are found (Fig. 2D). They form subcentimetre alternations of typical uncompacted AAD. Based on the extracted 16S rRNA gene sequences, the aragonite lamina host a similar archaeal community to the immediately overlying mat crust (Thomas *et al.*, 2015). However, the bacterial community seems more diverse, with halophilic fermenters such as *KBI Candidate Division* and *Halanaerobiaceae*, and rare *Desulfohalobium*-related organisms (halophilic sulphate reducer).

A cube of sediment was cut using sterile implements, immediately wrapped in Parafilm® M and stored at −4°C. Subsampling was done using a sterile scalpel and picks for various microscopy analyses in the geomicrobiology laboratory at the Department of Earth Sciences, University of Geneva.

The core material was taken from ICDP hole 5017-1A drilled during the DSDDP expedition. This core was retrieved in November-December 2010 from the middle of the Dead Sea (N 31°30′28·98″, E 35°28′15·60″) at a depth of 297 m. The core material was sampled either onshore from core-catchers at a specially tailored geomicrobiology laboratory, at Ein Gedi, Israel, or during the core-opening parties at GFZ Potsdam, Germany in June, 2011. In all cases, the outermost parts of the samples were discharged in order to avoid oxidation effects and contamination with drilling fluids.

METHODS

Scanning electron microscope

Samples were examined on smear slides after ethanol drying by use of an optical microscope. Halite samples were

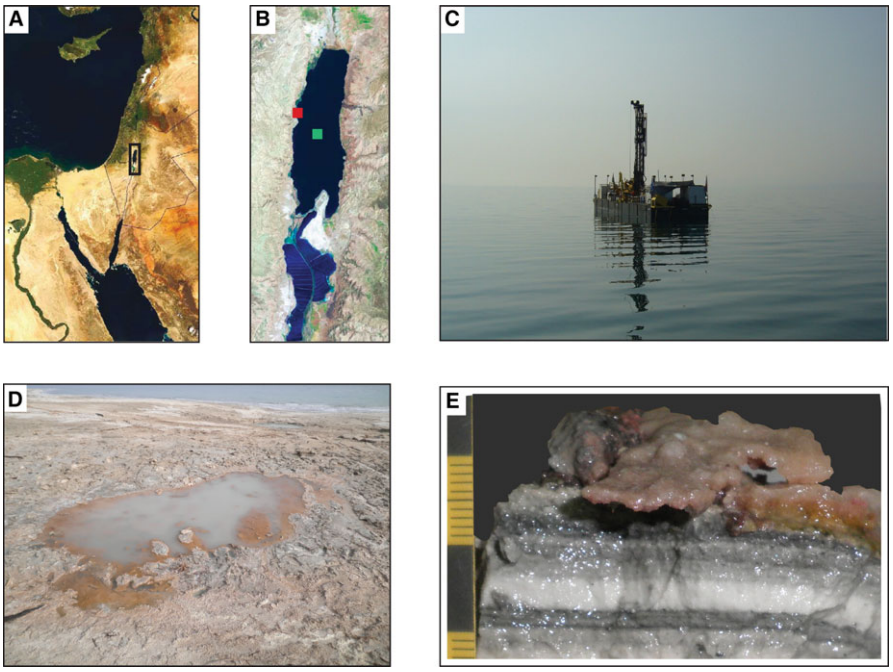

Fig. 1. Overview of sampling sites and material. (A) Map of the Levantine region with Dead Sea location. (B) Location of drilling site 5017-1A (green square) and of the Qedem area, where the microbial mat was sampled (red square). (C) View of the ICDP-drilling platform at site 5017-1A. (D) Hypersaline pond north of Ein Qedem, where the microbial mat sample was taken. The pool is *ca* 15 m long. (E) Photograph of the mat (red, orange and green in colour) with underlying laminated sediments (grey to white).

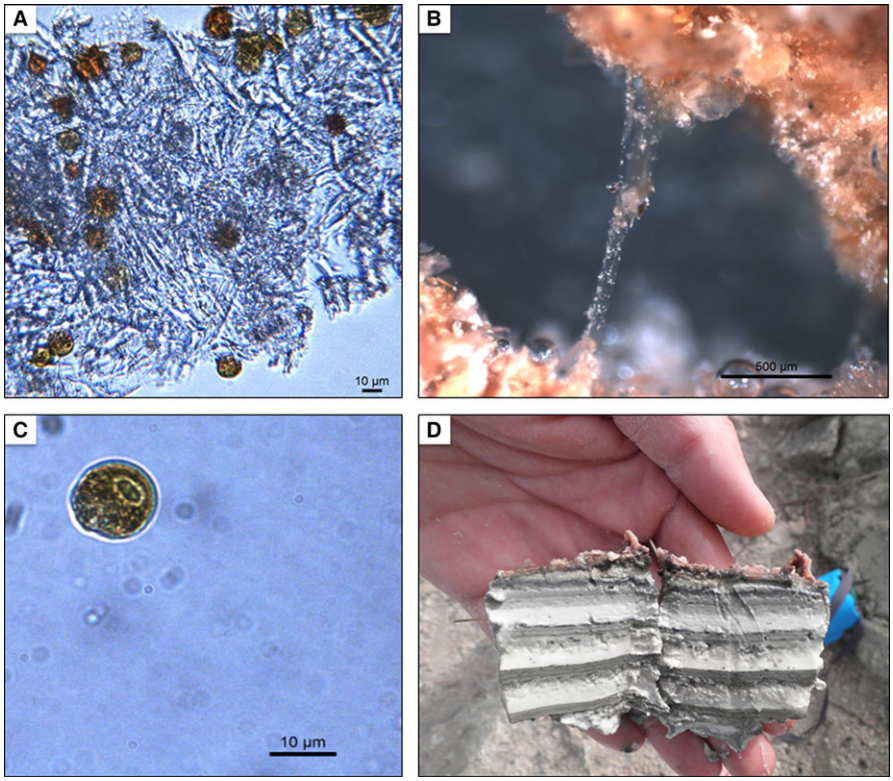

Fig. 2. (A) Aragonite needles and Dunaliella (orange circles) in the water of the ephemeral pond in Ein Qedem. (B) Photograph of EPS thread within a cavity of the gypsum-halite mat crust. (C) Close-up view of Dunaliella algae. Note that the nucleus is visible. (D) Section of the mat and underlying sediment exhibiting the AAD behaviour typical of the Lisan Formation.

already dry and were only polished with sand paper and clean alcohol. Scanning electron microscopy (SEM) was performed after ethanol and air drying, and critical point drying on a Jeol® JSM-7001 FA at the University of Geneva. Samples were then mounted on an aluminium stub with double-sided conductive carbon tape and gold-coated (15 nm) by low vacuum sputter coating.

Cryo-SEM was performed at C-SEM, in Neuchâtel, Switzerland on a Philips XL30 ESEM –FEG equipped with a Gatan Alto cryo-transfer system. The microscope was operated at 20 kV under a pressure of less than 10^{-4} mbar. The sample was freeze-dried in liquid nitrogen, transferred to the cryo-chamber stabilized at −140°C, where it was sectioned perpendicularly to the mat and sediment laminae using a blade, sublimated and sputtered with platinum. The sectioned surface was then observed.

Polished halite sections were examined using an Environmental Scanning Electron Microscope (ESEM) FEI Quanta 200 at the Scientific and Technological Centers, Universitat de Barcelona (CCiTUB). Chemical identification was performed by EDS.

Energy dispersive X-ray spectrometry (EDS) and back-scattered electron microscopy were used for chemical analysis on SEM, ESEM and cryo-SEM, allowing semi-quantitative determination of mineral chemistry.

X-ray fluorescence

Mapping of different elements within a section of microbial mat was performed using micro X-ray fluorescence (µXRF) at the University of Geneva under an EAGLE µProbe machine with a rhodium tube at a voltage of 40 kV and a current of 420 µA with a 50 µm spot. Mineral distribution was then interpreted based on each image and relative colour intensity using the software of the Adobe® Collection Suite and the Vision32® software version 4·953.

Elemental composition of core 5017-1A was measured using XRF at GFZ Potsdam, Germany on an ITRAX corescanner of COX Analytical Systems. A chromium tube was used at 30 kV and 30 mA. These data only allow for qualitative interpretations as they originate from raw counts (in counts per seconds) with sufficient counting statistics from un-calibrated quick core section scans as detailed by Neugebauer *et al.* (2014).

Electron microprobe

Magnetic fractions were collected as follows: sediment samples were extracted using plastic cubes, gathered using a magnetic probe and mounted in epoxy. The samples were analysed using a JEOL JX8230 superprobe EPMA with EDS and four wavelength-dispersive spectrometers (WDS) for microanalysis at the Institute of Earth Sciences, Hebrew University of Jerusalem. Both back-scattered electron (BSE) and secondary electron images were taken. Beam conditions for EDS analysis were set to 15 keV and 15 nA, and for WDS mapping 15 keV and 50nA. All phases were analysed for titanium, iron, sulphur, and oxygen using silicate and oxide standards. Data were processed with a PRZ correction procedure. The WDS measurement error is 0·5%. The difference between greigite and pyrite is bigger, than the error. Beam precision is 0·2 μm, allowing small crystals to be measured (as compared with 1 μm for EDS). In addition to the standard mineral correction, a matrix correction for the epoxy was also performed.

RESULTS

X-ray microfluorescence scanning on the mat

The facies of the microbial mat and its underlying sediment are similar to those defined in the cores (Neugebauer *et al.*, 2014). Halite mixed with gypsum is analogous to that of interglacial periods, except that it is completely embedded in EPS. Aragonitic laminae alternating with detritus show identical distribution to those of the AAD facies. The chemical compositions of the laminae are highlighted by key elements (Fig. 3). Chlorine is present in high and homogenous concentrations in the sediment and halite precipitated on the surface of the section (topography image) as the sample dried while being mapped at high resolution. Sulphur is concentrated in two laminae, and correlates with the strongest calcium peaks, indicating the presence of gypsum minerals. As with chlorine, the distribution of calcium (green) within the sediment is relatively homogeneous as it is highly concentrated in the Dead Sea water. Higher fluorescence of calcium corresponds to gypsum minerals. Aragonite is best mapped with strontium, showing the presence of aragonitic precipitation in light grey to white laminae of the mat (light blue in μXRF). It is intercalated by detrital input mapped under iron bands (light yellow). Diffuse detritus is also present below this band, imparting a greyish colour to the aragonite laminae. The 'Fe × S' mapping allows the areas of greatest iron sulphide mineralization to be highlighted. Although some background noise is observed due to the superposition of a gypsum and detritus signature, higher fluorescence identifies iron sulphide minerals, as pyrite, greigite or other transition phases and is represented in blue in the sketch (Fig. 3). The main iron-sulphur phases are observed at the margins of the detrital lamina, within the aragonite laminae, rather than within the iron-rich detritus lamina itself.

X-ray fluorescence scanning in the core

In the core, detailed XRF profiles highlight the lithologies and associated facies (further detailed in Neugebauer *et al.*, 2014). The 'Fe × S' curve is superimposed over the sulphur profile of core 1A, in order to emphasize areas of iron-sulphur mineralization (Fig. 4). Sulphur peaks are mainly seen in gypsum levels and sulphur concretion-rich intervals. In some cases (e.g. 100 m, 110 m, 160 m, 340–350 mblf), the high 'Fe × S' signatures of sulphur concretions overlap with the signal generated by iron-sulphur minerals as figure resolution does not allow for differentiation on a centimetre scale. Higher 'Fe × S' peaks are found between 0 and 80 m, especially within the 45 to 75 m interval where the 'Fe × S' profile does not always correlate with the sulphur curve, hence indicating other signatures than gypsum and native sulphur concretions (i.e. iron sulphide minerals). In general, the intensity is lower for 'Fe × S' profiles below 100 m, regardless of measured sulphur fluorescence. Examples of the morphologies and size of iron sulphide minerals are presented on the right side of Fig. 4, together with the corresponding EDS spectra.

Morphology of iron-sulphur phases

The chemistry and morphology of iron-sulphur minerals varies independently of depth. Euhedral minerals forming an octahedron have been found at a depth of 65·38 m (Fig. 5A) in the 'laminated detritus' facies (*ld*, Neugebauer *et al.*, 2014). Micron-scale spheroids were also found in such facies and also in gypsum intervals at 90·64 m (Fig. 5B), while rough-surface spherulites ca. 5 μm in diameter were retrieved at 337·62 m in the AAD (Fig. 5C).

Euhedral pyrite, typically 5 to 20 μm in diameter, occurs at the boundary between the detrital and aragonitic layers of the microbial mat (Fig. 5A). Core examples are much smaller. They are generally individual euhedrons of 5 μm maximum, sometimes presenting overgrowth (Fig. 5B). True pyrite framboids were observed in the mat (Fig. 5C) and consist of small octahedrons. In the core, framboids are rare and of limited size. They are formed of aggregated micro-spheroids (Fig. 5D) or crystals (Fig. 5E and F). This form may be a precursor phase of micron-scale spherules or larger rough-surface spherulites (Fig. 5G and H, respectively).

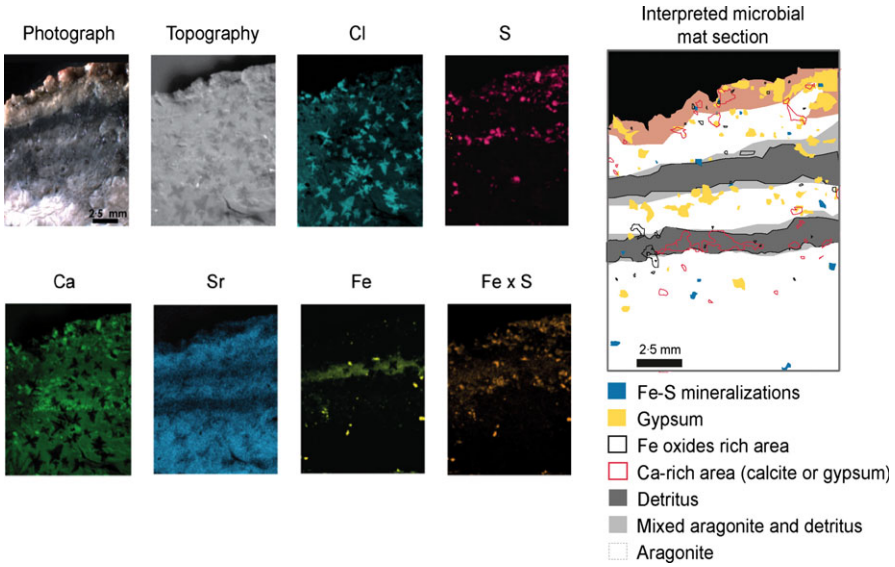

Fig. 3. Micro-XRF mapping of a microbial mat and the laminated sections of modern sediments along the Dead Sea shore. The dominant mineral is authigenic aragonite (Sr-mapping) with some gypsum (S and Ca). The darker layer is detrital material (calcite and clays). Disseminated Fe-sulphide is outlined by the 'Fe × S' mapping, and is principally found in aragonitic layers. Star shaped crystals are the result of secondary precipitation caused by desiccation of the samples during measurement. See Methods for details on the interpreted sketch. Scale bar is the same for each scanned image and is 2·5 mm.

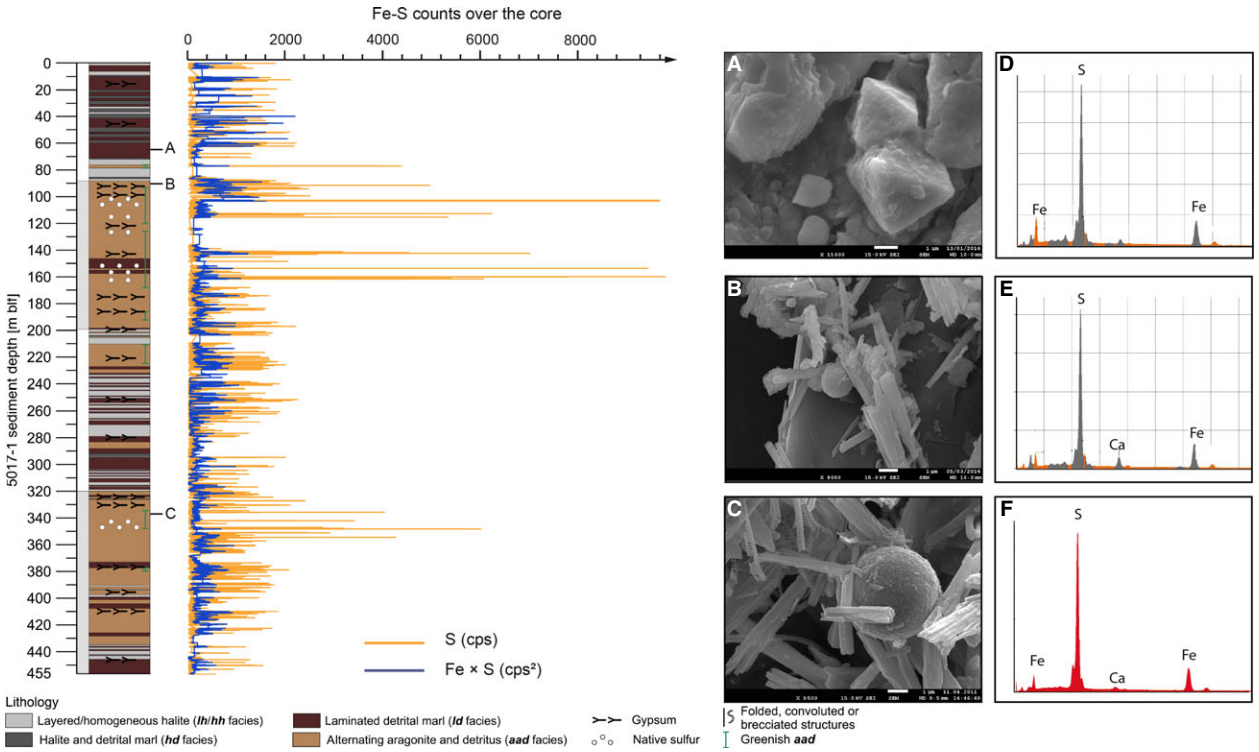

Fig. 4. Interpreted lithological profile of core 1A taken from Neugebauer *et al.* (2014) and corresponding S and Fe × S profiles as given by XRF scanning. On the right hand, SEM photographs of (A) micron-sized euhedral Fe-S mineralization from core 1-A-32 at 65·38 m. (B) Fe-S spheroid at 90,64 m, core 1-A-43. (C) rough- surface spherulite from core 1-A-131 at 337·62 m with the corresponding EDS spectra (D, E and F respectively). Depth in metres below lake floor.

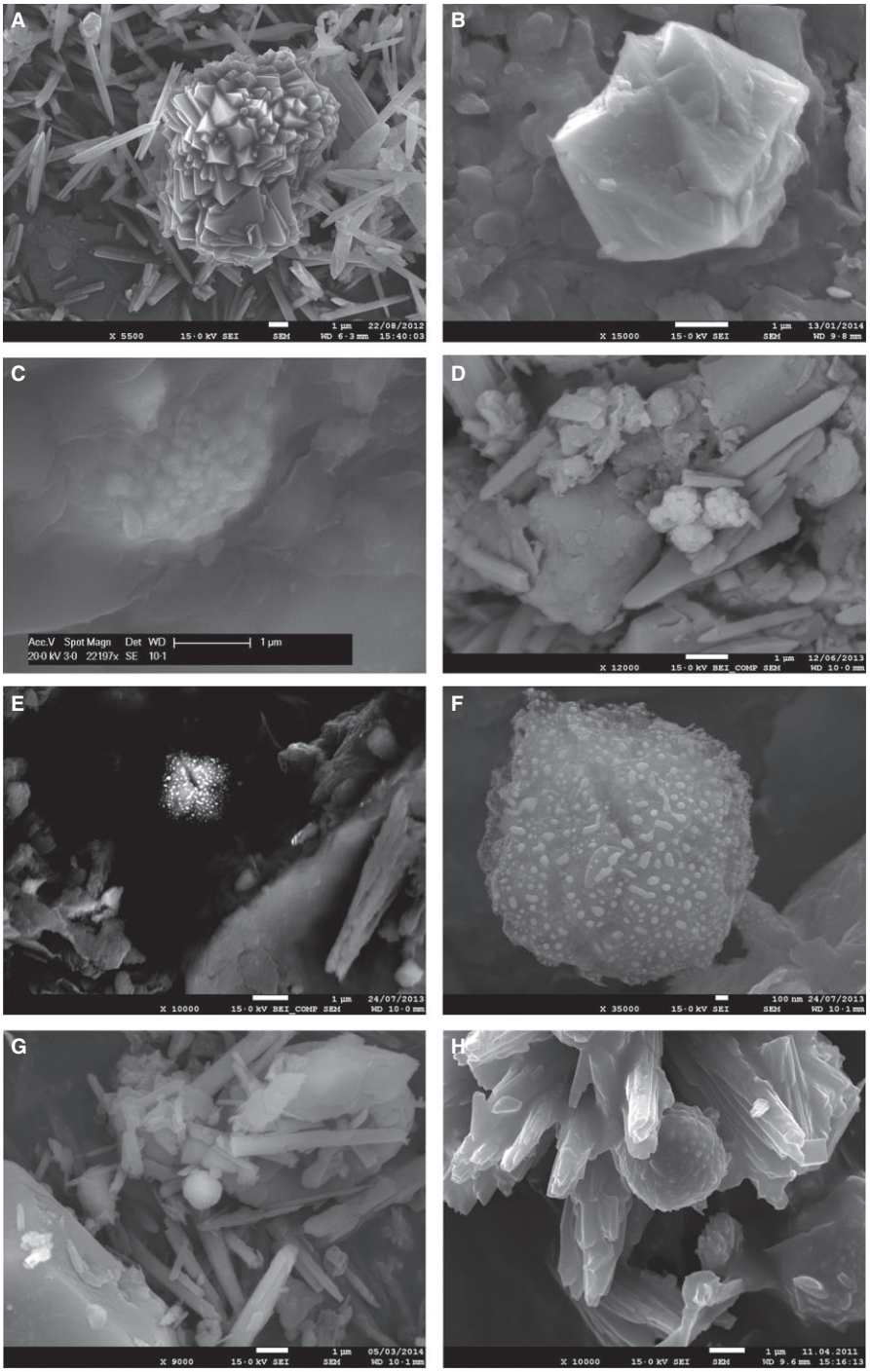

Fig. 5. Iron-sulphur mineralization morphologies in the Dead Sea realm. (A) Euhedral pyrite from a white aragonitic lamina of the mat. Aragonite needles are visible in the background. (B) Similar euhedral morphology of Fe-S mineral in core 1-A-32, at 65·38 mblf. (C) Cryo-SEM picture of a framboidal pyrite embedded in EPS at the mat-sediment interface of the mat sample. (D) Agglomerate of four framboidal mineralizations in the core (65·38 mblf). (E) Back-scattered electron imaging of a Fe-S rough-surface spherulite being formed in core 1- A-30, at 59·29 mblf. (F) Close-up view of (E) in secondary electron imaging, emphasizing the rough droplet like topography of the mineralization. (G) Micron-scale Fe-S spheroid at 90·64 mblf, core 1-A-43. (H) Rough surface spherulite of micron scale at the tip of aragonitic stellate cluster in core 1-A-131, at 337·62 mblf. Pictures were all taken under secondary electron imaging in a regular SEM, except when specifically stated.

Chemistry of iron-sulphur phases

In the core, iron-sulphur minerals rarely reach the iron-sulphur ratio characteristic of pyrite (S/Fe = 2; Table 1 and Fig. 6) except for the largest examples (> 5 μm), which approach true pyritic compositions (FeS_2). They are either euhedral minerals in the mat (Fig. 5A), or rough-surface spherulites at 350 m in the core (Fig. 4C).

In some dark, high magnetic susceptibility laminae associated with AAD (Fig. 7A), iron sulphide rims with a composition of greigite are observed around some titanomagnetite grains (Fig. 8). The titanomagnetite appears partially dissolved and iron-sulphur minerals also form on cracks. The composition of the iron-sulphur rim varies from greigite to pyrite depending on depth. Such rims are found both in the Holocene interglacial sediment and in the Lake Lisan-associated sediment (last glacial period). Greigite is also observed infilling chambers of organisms (e.g. foraminifera) in the Holocene AAD sediment (Fig. 9). Measurements of the atomic ratio of these intra-skeletal iron-sulphur minerals revealed S:Fe values between 1·32 and 1·35, characteristic of greigite (Fig. 9 and Table 1). Except in the mat, EDS and WDS measurements show rather continuous S/Fe ratios, with higher values (pyrite-like) attributed to deep AAD samples (140–151 m, 337 m) and mackinawite to greigite chemistry for others (Table 1 and Fig. 6).

Although not fully characterized, iron-sulphur mineral phases also occur around gypsum in detrital-rich halite intervals (Fig. 10 and Table 1). Most of the other minerals, generally in the form of spherules or octahedrons, have a similar chemistry to greigite (Fe_3S_4). Few iron-sulphur precipitates lie below the mackinawite line (Fe_8S_9), and they are sub-micron in size. The resolution for EDS spot analysis is superior to 1 μm in length and width. Data from smaller minerals should be considered with caution and have been highlighted in Fig. 6.

Microscopic analysis of EPS

Exopolymeric substances have been clearly observed in the mat, with the naked eye, as well as with a regular microscope (Fig. 2) and with cryo-SEM. A cerebroid structure under cryo-SEM facilitates EPS identification in the mat (Fig. 11A) together with a transparent film-like texture in close-up view, frequently with embedded aragonite stellate clusters (Fig. 11B). This texture differs from the characteristic honeycomb morphology generally observed in cryo-SEM sections (Defarge *et al.*, 1996; Dupraz *et al.*, 2004). This difference is interpreted as being a result of the extreme salinity of the Dead Sea.

In regular SEM mode, the EPS are very smooth and appear transparent, often covering the sediment (Fig. 11C). The EPS in the core have a filmy texture, sometimes folding in on itself, or torn apart during preparation (Fig. 11D), possibly presenting voids and more rugged surfaces. Aragonitic stellate clusters or individual needles are often found embedded in these EPS.

Cryo-SEM observations of the mat sample allowed sharp, freshly precipitated aragonite stellate clusters to be distinguished embedded in the cerebroid texture typical of the EPS (Fig. 12A). The thin needles constituting the stellate cluster are individually covered by the biofilm in close-up view (Fig. 12B). Rough surfaces on the torn EPS are formed by nanoglobules (Fig. 12C). They are also visible between aragonitic needles, apparently entangled in this biological structure (Fig. 12D). The needles here are very thin and elongated, without sharp tips nor smooth surface. In the core, sharp and thin aragonite stellate clusters, as well as fragments of thick ones may emerge or pierce through the EPS (Fig. 12E). They also are found aggregated on its surface (Fig. 12F), or in between EPS and gypsum minerals, where the EPS host numerous iron sulphide minerals, as demonstrated by back-scattered imaging (Fig. 12G). At depths greater than 20 mblf (Table 1), EPS-like structures could not be identified although smooth film-like textures were found associated with aragonitic stellate clusters (Fig. 12H). Here, they correspond to halite minerals, demonstrating the complexity of untangling biotic features from abiotic ones in the Dead Sea sediment.

DISCUSSION

Indicators of microbial activity in the Dead Sea sediment

EPS

Examples of EPS are well represented within the microbial mat (Fig. 2B and D). Their recognition is generally difficult in the wet Dead Sea sediment. Numerous poorly investigated precipitates, occurring in the Dead Sea naturally or upon desiccation before SEM observation, may take on a smooth sheet-like structure (Fig. 11H) similar to documented textures for EPS (Spadafora *et al.*, 2010). Chemical analysis of hypothesized EPS is not equivocal as X-ray penetration of EDS generally exceeds the EPS thickness. Loading of these structures with calcium, magnesium and chloride also tends to mask its carbon and oxygen content (Fig. S1 of Supplementary Material). Morphological characterization of EPS, therefore, was often the most reliable solution and analysis of chemical composition and morphology under cryo-SEM mode allowed for conclusive identification.

In the core, EPS are also observed. However, their observation is limited mainly to the top of the core

Table 1. Summary of the samples observed and measured under scanning electron microscope (SEM), environmental scanning electron microscope (ESEM) and electron microprobe (EPMA). Changes in shade mark changes in sample (hence in depth).

Core (5017-A)	Depth (mblf)	Lithology	Type of analysis	S/Fe ratio	EPS observed
1-1	0	lh/hh	ESEM	?	n/a
1-1	0,24	lh/hh	SEM	–	Yes
2-2	2,74	aad	EPMA	1,36	Yes
2-2	2,74	aad	EPMA	1,32	
2-2	2,74	aad	EPMA	1,30	
2-2	2,74	aad	EPMA	1,36	
2-2	2,74	aad	EPMA	1,30	
2-2	2,74	aad	EPMA	1,31	
2-cc	3,29	lh/hh	SEM	?	No
3-cc	6,34	lh/hh	SEM	?	No
5-cc	9,39	lh/hh	SEM	?	No
13-cc	23,59	ld	SEM	?	Yes
29-cc	57,26	gy	SEM	1,25	No
29-cc	57,26	gy	SEM	0,69	
30-cc	59,29	ld	SEM	1,08	No
30-cc	59,29	ld	SEM	1,30	
30-cc	59,29	ld	SEM	1,33	
30-cc	59,29	ld	SEM	1,33	
30-cc	59,29	ld	SEM	1,38	
30-cc	59,29	ld	SEM	0,79	
30-cc	59,29	ld	SEM	1,08	
30-cc	59,29	ld	SEM	0,86	
30-cc	59,29	ld	SEM	1,30	
30-cc	59,29	ld	SEM	1,33	
30-cc	59,29	ld	SEM	1,50	
30-cc	59,29	ld	SEM	1,38	
30-cc	59,29	ld	SEM	1,08	
30-cc	59,29	ld	SEM	0,79	
32-cc	65,38	aad	SEM	0,59	No
32-cc	65,38	aad	SEM	1,23	
32-cc	65,38	aad	SEM	1,42	
32-cc	65,38	aad	SEM	1,17	
32-cc	65,38	aad	SEM	1,46	
32-cc	65,38	aad	SEM	1,23	
32-cc	65,38	aad	SEM	1,61	
32-cc	65,38	aad	SEM	1,37	
32-cc	65,38	aad	SEM	1,33	
32-cc	65,38	aad	SEM	1,46	
32-cc	65,38	aad	SEM	1,38	
32-cc	65,38	aad	SEM	1,40	
32-cc	65,38	aad	SEM	1,35	
32-cc	65,38	aad	SEM	1,45	
32-cc	65,38	aad	SEM	1,69	
32-cc	65,38	aad	SEM	1,68	
32-cc	65,38	aad	SEM	1,47	
32-cc	65,38	aad	SEM	1,22	
32-cc	65,38	aad	SEM	1,45	
32-cc	65,38	aad	SEM	1,14	
32-cc	65,38	aad	SEM	1,66	
32-cc	65,38	aad	SEM	0,95	
32-cc	65,38	aad	SEM	1,46	
32-cc	65,38	aad	SEM	1,47	
32-cc	65,38	aad	SEM	1,19	
32-cc	65,38	aad	SEM	0,98	
32-cc	65,38	aad	SEM	1,72	
33-cc	67,38	ld	SEM	1,24	No
33-cc	67,38	ld	SEM	1,45	
33-cc	67,38	ld	SEM	1,22	
33-cc	67,38	ld	SEM	1,57	
33-cc	67,38	ld	SEM	0,97	
33-cc	67,38	ld	SEM	1,47	
33-cc	67,38	ld	SEM	1,59	
33-cc	67,38	ld	SEM	1,40	
33-cc	67,38	ld	SEM	1,63	
33-cc	67,38	ld	SEM	1,36	
33-cc	67,38	ld	SEM	1,06	
33-cc	67,38	ld	SEM	1,40	
33-cc	67,38	ld	SEM	1,48	
33-cc	67,38	ld	SEM	1,64	
33-cc	67,38	ld	SEM	1,49	
33-cc	67,38	ld	SEM	1,25	
33-cc	67,38	ld	SEM	1,06	
33-cc	67,38	ld	SEM	1,14	
33-cc	67,38	ld	SEM	1,31	
33-cc	67,38	ld	SEM	1,33	
36-1	73,425	lh/hh	ESEM	–	n/a
37-2	75,425	lh/hh	ESEM	?	n/a
37-cc	75,58	ld	SEM	1,59	no
37-cc	75,58	ld	SEM	1,00	
37-cc	75,58	ld	SEM	0,56	
37-cc	75,58	ld	SEM	1,51	
37-cc	75,58	ld	SEM	1,22	
37-cc	75,58	ld	SEM	0,72	
37-cc	75,58	ld	SEM	0,42	
40-1	82,8	lh/hh	ESEM	?	n/a
41-1	85,445	lh/hh	ESEM	–	n:a
43-cc	90,64	gy	SEM	1,45	No
43-cc	90,64	gy	SEM	1,62	
52-cc	118,08	ld	SEM	1,39	No
52-cc	118,08	ld	SEM	1,45	
53-cc	121,13	ld	SEM	–	No
60-3	142,88	ld	EPMA	2,19	n/a
60-3	142,88	ld	EPMA	1,21	n/a
61-1	144,08	ld	EPMA	1,94	n/a
61-1	144,08	ld	EPMA	1,98	
61-1	144,08	ld	EPMA	1,88	
61-1	144,08	ld	EPMA	1,75	
61-1	144,08	ld	EPMA	1,66	
61-1	144,08	ld	EPMA	1,73	
61-3	146,13	aad	EPMA	1,85	n/a
61-3	146,13	aad	EPMA	2,25	
61-3	146,13	aad	EPMA	2,29	
61-3	146,13	aad	EPMA	2,24	
61-3	146,13	aad	EPMA	1,98	
61-3	146,13	aad	EPMA	1,97	
61-3	146,13	aad	EPMA	2,31	
61-3	146,13	aad	EPMA	2,35	

(*Continued*)

(*Continued*)

Table 1. Continued.

Core (5017-A)	Depth (mblf)	Lithology	Type of analysis	S/Fe ratio	EPS observed
61-3	146,13	aad	EPMA	2,30	
61-3	146,13	aad	EPMA	2,11	
63-3	151,47	ld	EPMA	1,83	n/a
63-3	151,47	ld	EPMA	2,01	
63-3	151,47	ld	EPMA	1,95	
63-3	151,47	ld	EPMA	1,85	
63-3	151,47	ld	EPMA	0,94	
63-3	151,47	ld	EPMA	1,82	
63-3	151,47	ld	EPMA	2,03	
63-3	151,47	ld	EPMA	2,01	
80-1	199,175	lh/hh	ESEM	–	n/a
81-2	202,935	lh/hh	ESEM	?	n/a
88-2	224,6	ld	SEM	?	no
91-2	233,38	lh/hh	ESEM	?	n/a
91-2	233,52	lh/hh	ESEM	?	n/a
93-1	236,2	lh/hh	ESEM	–	n/a
93-1	237,03	lh/hh	ESEM	?	n/a
95-1	241,41	lh/hh	ESEM	–	n/a
97-2	248,24	lh/hh	ESEM	?	n/a
97-2	248,43	lh/hh	ESEM	?	n/a
98-2	250,665	lh/hh	ESEM	–	n/a
98-3	253,052	lh/hh	ESEM	–	n/a
100-2	254,82	lh/hh	ESEM	–	n/a
100-cc	256,955	lh/hh	ESEM	?	n/a
103_3	263,383	lh/hh	ESEM	–	n/a
104-2	266,5	lh/hh	ESEM	?	n/a
106-2	272,21	lh/hh	ESEM	–	n/a
108-2	278,534	lh/hh	ESEM	?	n/a
125-1	319,865	lh/hh	ESEM	?	n/a
125-1	319,93	lh/hh	ESEM	?	n/a
131-cc	337,62	aad	SEM	1,77	no
131-cc	337,62	aad	SEM	1,93	
174-1	437,59	lh/hh	ESEM	–	n/a
174-1	438,84	lh/hh	ESEM	?	n/a
176-2	445,35	lh/hh	ESEM	?	n/a
176-2	445,7	lh/hh	ESEM	?	n/a

Mat layer	Depth (mblf)	Lithology	Type of analysis	S/Fe ratio	EPS observed
Mat surface	0,01	ha-gy in EPS	SEM	?	Yes
Mat detrital	0,06	aad	SEM	2,04	Yes
Mat aragonite	0,16	aad	SEM	2,03	No
Mat aragonite	0,16	aad	SEM	1,98	No

S/Fe ratios were calculated after EDS measurements for SEM and WDS measurements for EPMA. They were not calculated on ESEM but are annotated '?' when iron sulphides were observed, and 'no' when no iron sulphide phases could be found. EPS presence/absence is given for the observed samples on SEM. They were not looked for using ESEM and EPMA (n/a). Depth is in metres below lake floor. Lithology codes are described in Neugebauer *et al.* (2014). Lh/hh layered and homogenous halite, hd halite and detrital marl, aad alternating aragonite and detritus, ld laminated detrital marl, gy gypsum laminae or layers. For comparison, stoichiometric ratios of iron sulphide minerals are: $S/Fe_{pyrite} = 2$; $S/Fe_{greigite} = 1{,}33$; $S/Fe_{mackinawite} = 0{,}89$.

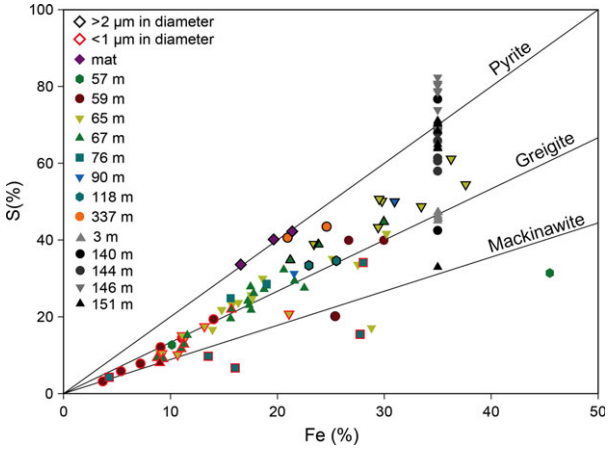

Fig. 6. Iron-sulphide mineral compositions taken from EDS measurements (colour) and EPMA (black and grey). The microprobe ratios have been normalized to a given iron percentage (35%) for better understanding. EDS measurements from small minerals (<1 µm) are circled in red to stress the bias induced by this type of measurements on micron-sized objects (see Methods). Pyrite line as y = 1/2(x), greigite line as y = 3/4(x) and mackinawite line as y = 9/8(x).

(Table 1) with minimal recognition below that. Extraction of EPS was attempted but did not work as a large quantity of salt was carried along in the process, inducing a large bias analytically. The failure to identify EPS below 23 m suggests either (i) that they were missed, (ii) degradation with time in the deeper sediment or (iii) difference/absence of production in the first place. The finding of EPS in the upper part of the core suggests that microbial activity has occurred at one point in the sediment. Their disappearance deeper in the core may also support anaerobic heterotrophy.

Protection from the high calcium and magnesium divalent cation concentrations is probably the main reason for EPS production in the Dead Sea. The bonding capacity of EPS towards divalent cations (Kawaguchi & Decho, 2002; Dupraz & Visscher, 2005) could lower *in situ* concentrations of these cations, which is the principal reason the Dead Sea is inimical to life (Nissenbaum, 1975; Bodaker *et al.*, 2010). The EDS measurements on EPS (Fig. S1 of supplementary material) show concentrations of calcium and magnesium in the EPS matrix; however, such measurements must be interpreted very carefully given analytical inaccuracy on such thin structures.

Iron sulphide minerals

In the microbial mat, several types of iron-sulphur minerals were observed. Framboidal pyrite was only located close to the mat while large euhedral pyrite occurred in the underlying aragonitic laminae (Fig. 3). In the core, however, although euhedral minerals were observed, they

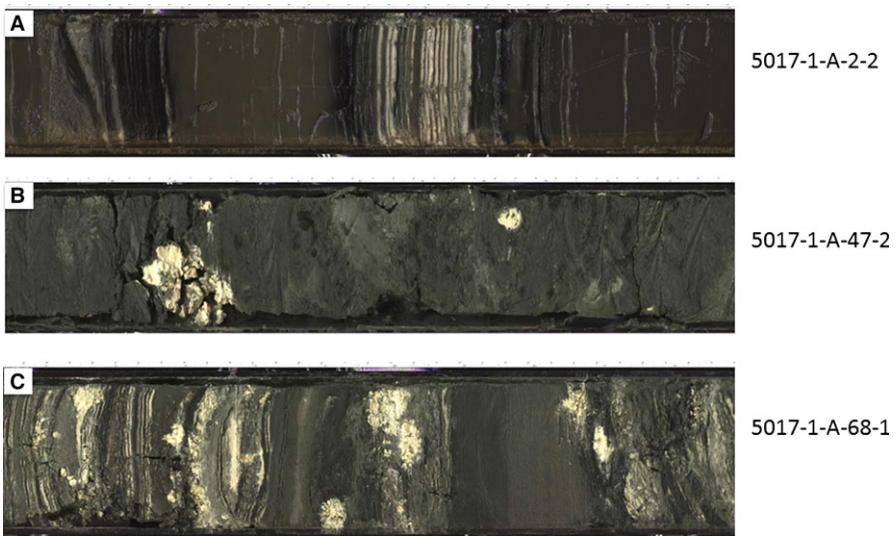

Fig. 7. Photographs of the cores. (A)Black layer exhibiting peaks in magnetic susceptibility and greigite occurrences near AAD intervals. (B) Isolated S^0 concretions in reworked intervals. (C) S^0 concretions in disturbed and undisturbed AAD.

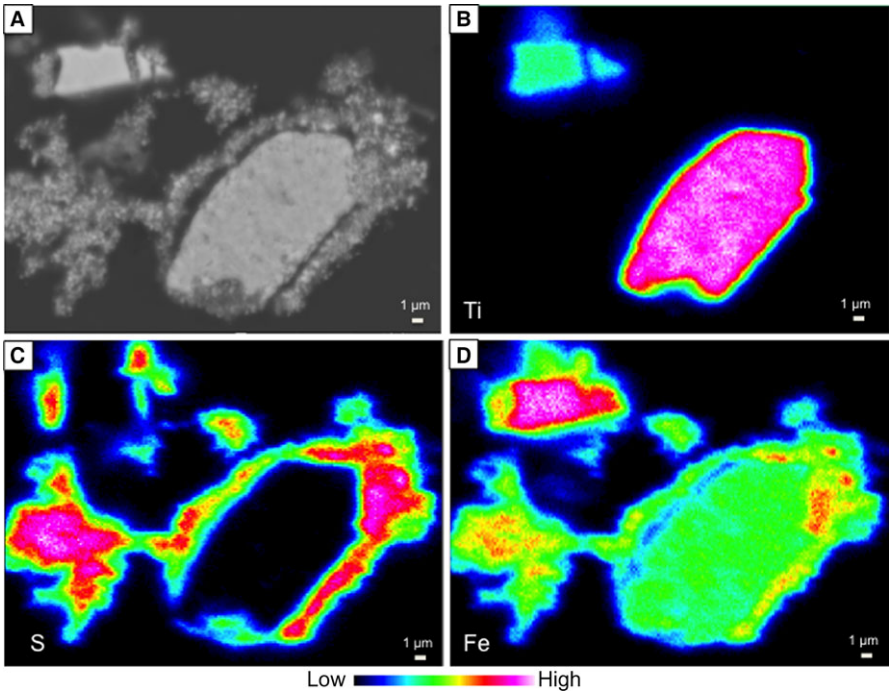

Fig. 8. Greigite rim around titanomagnetite in Holocene AAD sediment. (A) Back-scattered electron image. (B) WDS mapping of relative distribution of titanium highlights the titanomagnetite mineralogy. An outward depletion is observed at its rim. (C) WDS mapping of relative distribution of sulphur highlights the presence of Fe-S around the mineral (D) WDS mapping of relative distribution of iron shows enrichment in the Fe-S rim when compared to the internal chemistry of the titanomagnetite.

were generally small in size (<2 µm diameter). Their chemistry is also significantly different, with Fe/S ratios often limited to that of mackinawite or greigite (Fig. 6), and much less pyrite.

Linking morphology with formation processes is still a matter of debate. The composition and morphology of iron sulphide minerals results from numerous parameters such as the variety of reactive iron available, the

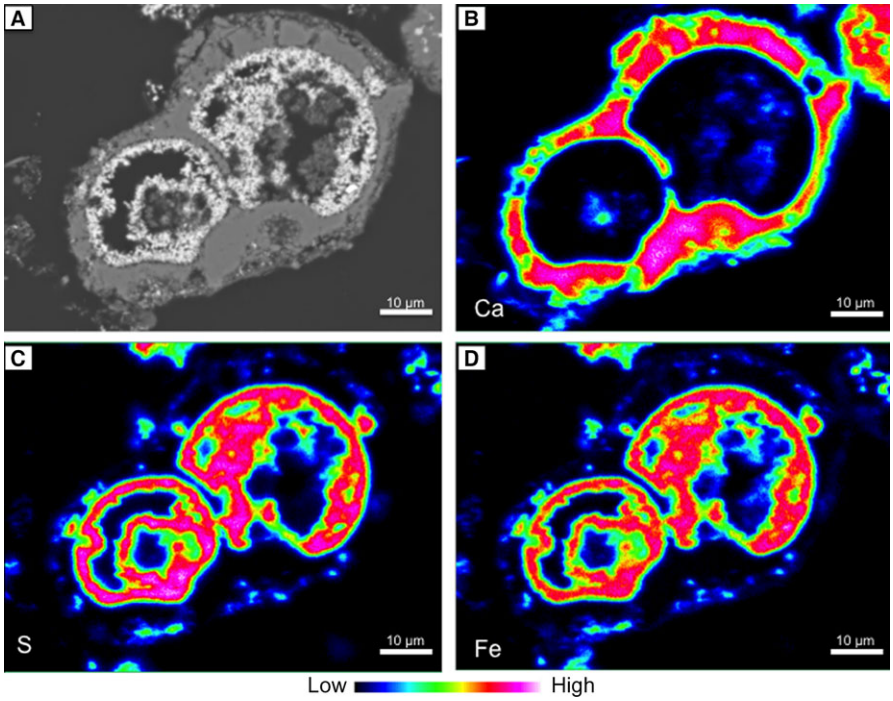

Fig. 9. Greigite and Fe-S infill within foraminifera. (A) Back-scattered electron imaging showing differences between the foraminifera lodges and its infill. (B) WDS mapping of relative distribution of Ca. (C) WDS mapping of relative distribution of S. (D) WDS mapping of relative distribution of Fe. Note the connection between the two chambers seen in (A). (C) sulphur and (D) iron concentrations mark the Fe-S mineral infilling, probably replacing the organic matter within the organism shell.

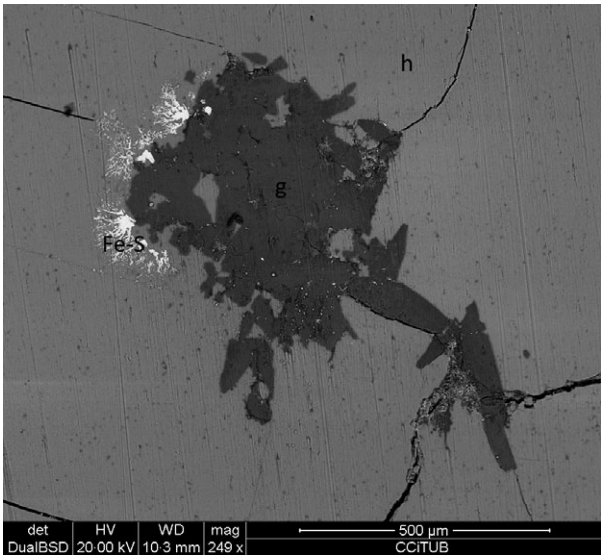

Fig. 10. Back-scattered electron photograph from SEM of a polished halite sample. Fe-S mineralizations develop around gypsum (g) inclusions within a halite (h) crystal.

saturation rate, the concentration of reduced sulphur and stability of redox conditions (Berner, 1984; Wang & Morse, 1996; Wilkin & Barnes, 1997; Wilkin & Arthur, 2001). A combination of observations from field and laboratory models attempting to mimic sedimentary processes have allowed characterization of framboidal, pentagonal, octahedral, tetrahedral, dodecahedral and icosahedral pyrite forms originating from biogenic factors (Astafieva *et al.*, 2005). This type of geometry encompasses all euhedral morphologies described above for the Dead Sea core and mat. Framboidal pyrites are formed of these euhedral structures as well as from micro-spheroids (Wilkin & Barnes, 1997), as observed in the core (Figs 4B and 5D), and have been demonstrated to be biomarkers in the sediment (Popa *et al.*, 2004; Vuillemin *et al.*, 2013).

Sulphate reduction has been indirectly documented in several studies of the Lake Lisan sediment (Gavrieli *et al.*, 2001; Torfstein *et al.*, 2005) and the stratified Dead Sea water column (Nissenbaum, 1975; Nissenbaum & Kaplan, 1976). Although less studied, microbial reduction of iron is also suggested as a source of ferrous iron in the sediment (Nishri & Stiller, 1984; Gavrieli *et al.*, 2001). Based on these observations, the presence of iron-sulphur minerals in the core of the Dead Sea argue for similar processes (microbial iron and sulphate reduction) in the deep Dead Sea Basin.

In addition, sulphur concretions were localized in the whole core (Neugebauer *et al.*, 2014). It is hard to explain their distribution as is seems that they occur both in well

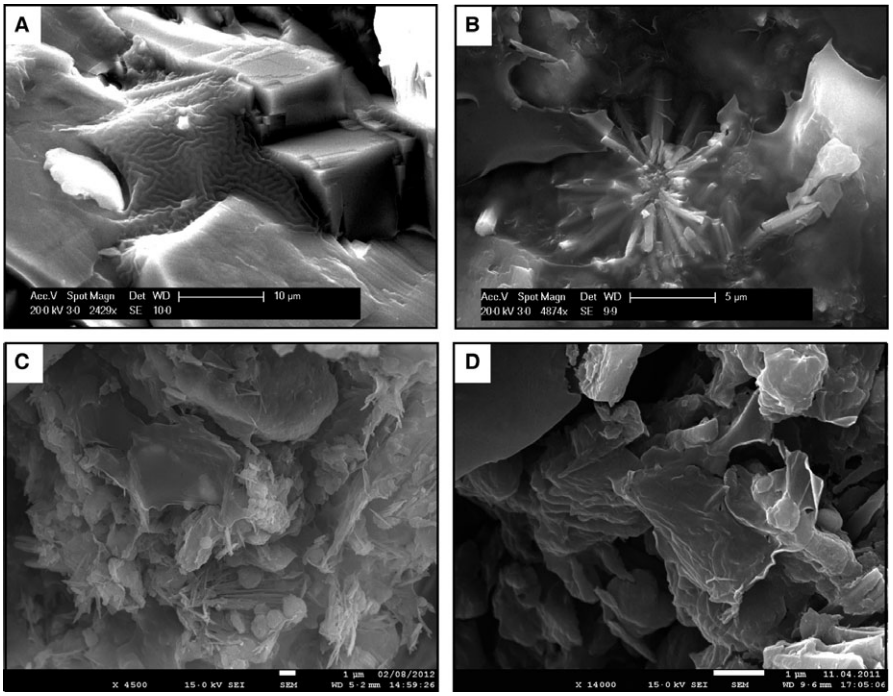

Fig. 11. Photographs of EPS morphologies in the mat (A) Cryo-SEM picture of EPS sheet in between gypsum crystals. Note the wrinkly cerebroid structure clearly defining the biofilm. (B) Cryo-SEM picture of an aragonite stellate cluster embedded in sheet-like EPS. (C) Regular SEM picture of sheet-like EPS covering detrital sediment. Globules are clay minerals, needles are aragonite. (D) Regular SEM picture of sheet-like EPS, torn and folded as it can occur in the core, here at 23·59 mblf in core 1-A-13.

preserved and in seismically disturbed AAD, as well as in mass wasting deposits (Fig. 7B and C). Different pathways can explain their formation, from incomplete sulphate reduction as suggested by Bishop *et al.* (2013) to oxidation of reduced sulphur species by turbidity events. Both pathways support the role of microbial sulphate reduction in the accumulation of sulphide or S^0 in the sediment of the Dead Sea Basin. The fact that the chemistry of iron sulphides does not systematically reach that of pyrite, and allows coexistence of greigite and pyrite, raises questions regarding the process of pyritization in this sedimentary environment. This issue is addressed in the next paragraphs.

Organic matter production and sulphate reduction

Microbial communities inhabiting the gypsum sediments are mainly composed of highly adapted halophilic *Archaea*, relying mostly on fermentation of varied organic substrates (Thomas *et al.*, 2014). Alternatively, communities inhabiting the AAD seem to rely on the degradation of biomass derived from moderate halophiles living within the stratified water column (Ariztegui *et al.*, 2015) and EPS production could be related to a stress response of these moderate halophiles. It could also originate from sulphate reducing microbes inhabiting these sediments, as they have been recognized to be important EPS producers (Bosak & Newman, 2005; Braissant *et al.*, 2007). Degradation of these EPS by fermenters or sulphate reducing bacteria may release organic molecules such as aminated compounds (Mishra & Jha, 2009). Such compounds would be subsequently available for osmoprotectant synthesis or uptake by community members utilizing a 'low-salt strategy' (Roesser & Müller, 2001). They could also support other communities such as methanogens as non-competitive substrate (Thomas *et al.*, 2014), enabling more activity and organic matter degradation.

In the microbial mat

The quality of organic matter is critical for microbial activity in deep lacustrine sediments (Glombitza *et al.*, 2013; Ariztegui *et al.*, 2015). In the Dead Sea, energy requirements for osmotic adaptation select for metabolisms yielding the largest amount of ATP for a given quantity of substrate (Oren, 2001). In such competition, labile substrates and nutrient availability have a major impact. Water column communities and shallow sedimentary ones, like those observed in the microbial mat,

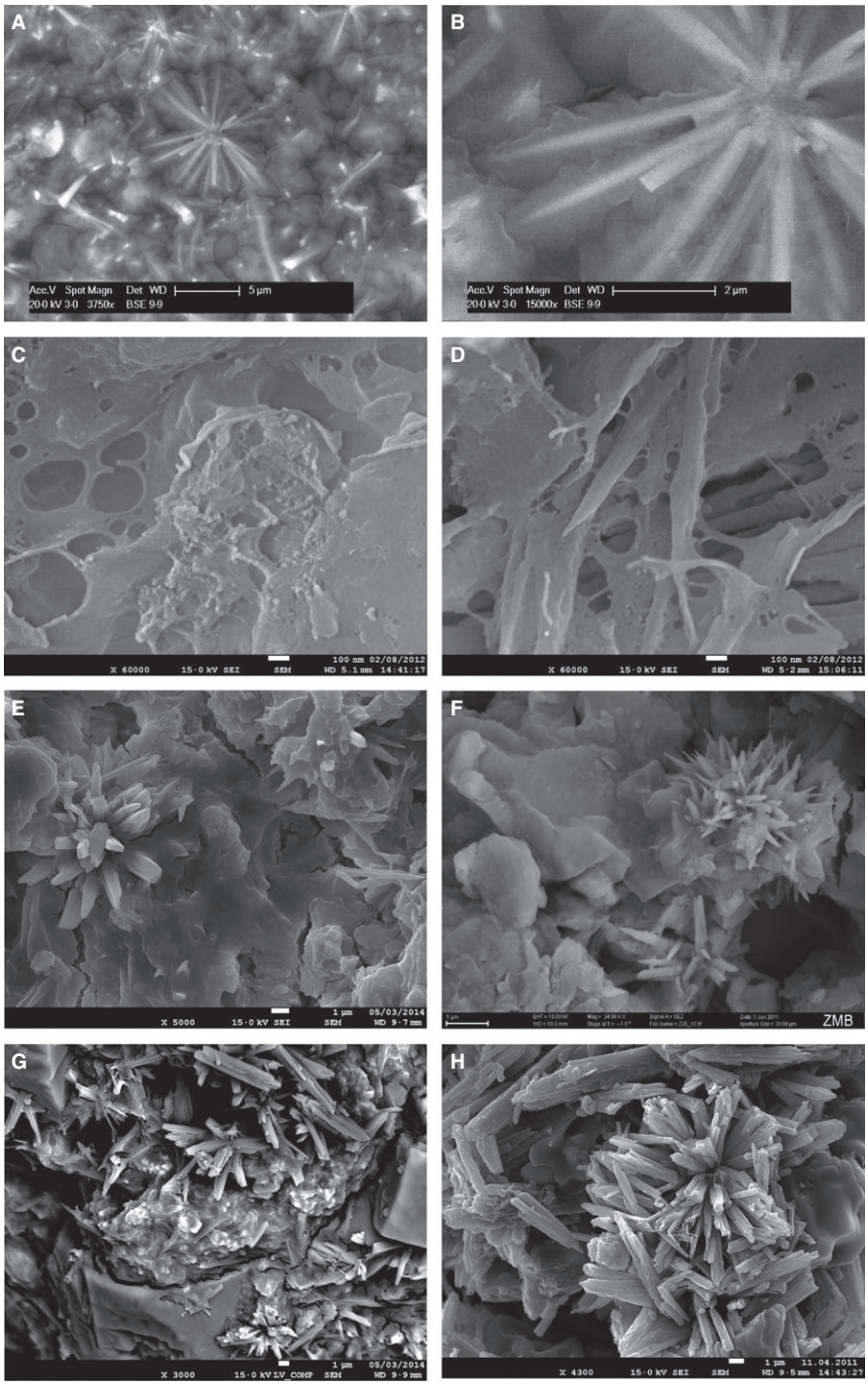

Fig. 12. Photographs of EPS structures in the mat and the core. (A) Cryo-SEM back-scattered electron photograph of an aragonite stellate cluster embedded in wrinkly EPS. Close-up view (B) shows the tight relationship between aragonitic thin needles in the EPS matrix. (C) Nanoglobules on the surface of torn and folded EPS. In the back, EPS display vacuolar textures. (D) Aragonitic needles covered with EPS (as seen by torn and vacuolar textures) and with nanoglobule-like textures at their tips. Needles are thin, poorly defined and not smoothened here. (E-F) Aragonite stellate clusters embedded in EPS form core 1-A-2 at 2·74 mblf and 3·22 mblf. (G) Back-scattered electron imaging of Fe-S mineralizations embedded in EPS, in between aragonitic agglomerates (top) and gypsum mineral (bottom) from 2·74 mblf. (H) Aragonite stellate cluster at the surface of halite smooth surface at depth 337·62 mblf, in core 1-A-131. A-D from the mat, the rest from the core. All pictures taken in secondary electron imaging unless stated otherwise.

for example, will benefit from fresher and more labile organic matter and will subsequently be able to perform metabolic activity deeper ones cannot afford.

The mat microcosm benefits both from the presence of a salinity gradient and from fresh organic matter. Among others, *Dunaliella* algae probably developed and survived after fresh water inputs to a small, ephemeral pond (rain events occurred in December 2010; Fig. 2A and C). Mixing with Dead Sea water, dissolution of surrounding salt and evaporative process in such a shallow pond would quickly raise elemental concentrations to those observed at sampling time. The decay of these abundant autotrophs (Fig. 2A) provides highly labile organic matter to the shallow sedimentary community, allowing mat development. Such high-quality organic matter would encourage high rates of sulphate reduction, facilitating the formation of framboidal pyrite in its vicinity, as described by Passier *et al.* (1997) in the Mediterranean Basin. Indeed, framboids are only observed very close to the gypsum crust within the microbial mat, while large euhedral pyrite dominates in the aragonite layers.

Both microtextures have been shown to result from differential rates of pyritization (Wilkin & Barnes, 1996). In their demonstration of pyritization via iron loss from iron monosulphides, the authors show that fast pyritization leads to framboidal pyrite while euhedral crystals result from slow initial pyritization. Intense sulphate reduction in the microbial mat could allow framboidal pyrite to develop. Excess HS^- could diffuse away and react with iron monosulphide to form the large euhedral pyrites present in the aragonite lamina, at the interface with detrital layers (Fig. 3). Sulphur isotope measurements on iron-sulphur phases would allow testing for the formation of these minerals in open versus closed systems. The liberation of reduced iron derived from the neighbouring detritus layer would be sufficient to support the process of pyritization.

In the deep sediment

In the core, very few actual framboids were observed. Iron-sulphur minerals often occurred as micron-sized individual spherules, only rarely aggregating into framboids. At given intervals, euhedral iron-sulphur minerals similar (in morphology) to those observed in the mat, but often smaller in size, could be observed.

The chemistry of these iron-sulphur minerals extends from iron monosulphides to pyrite (Fig. 6 and Table 1). The smallest iron-sulphur phases have an iron-sulphur ratio between mackinawite and greigite. Iron monosulphides have been acknowledged as important precursors in the formation of pyrite (Berner, 1970; Canfield *et al.*, 1992; Wilkin & Barnes, 1996). Pyritization has been observed to occur through different pathways including: (i) the polysulphide pathway consisting of adding S^0 to the iron-sulphur precursor (Rickard, 1975; Luther, 1991); (ii) the ferrous iron loss pathway (Wilkin & Barnes, 1996) where oxidants such as O_2, nitrate, Fe(III), Mn(IV) or organic matter allow the release of a Fe^{2+} ion or (iii) the H_2S pathway consisting of a solid state reaction (Drobner *et al.*, 1990; Rickard & Luther, 1997; Pósfai *et al.*, 1998). Transformation of mackinawite to greigite, and greigite to pyrite necessitate similar reactants, although kinetic limitations highlighted by Hunger & Benning (2007) prevent the full transformation of mackinawite to pyrite in sulphur limiting conditions.

The data presented here are consistent with a pyritization process in which S^0 is added to iron-sulphur precursors and suggests a transitional path from mackinawite to greigite and eventually to pyrite in the Dead Sea core, with limiting S^0. Although no general rate can be observed since a clear correlation is not seen between pyrite content and depth, it seems that progressive sulphidation as suggested by Sweeney & Kaplan (1973) and Schoonen & Barnes (1991) allows pyrite formation in the Dead Sea. This sulphidation is most probably the result of microbial sulphate reduction in the Dead Sea sediment. Such a process has been identified in the present Dead Sea (Häusler *et al.*, 2014) where it can benefit from very sharp salinity gradients formed, for example, by underwater fresh water springs.

Sulphate reduction rates in the sediment are, however, supposed to be very slow because of the high salinity and low input of fresh carbon (Häusler *et al.*, 2014). It means that the production of sulphide from an allegedly infinite sulphate source in most of the deep Dead Sea sediment (as observed from gypsum saturation), is limited. Recently, Bishop *et al.* (2013) suggested that sulphate reduction in the Dead Sea sediment does not even proceed all the way to hydrogen sulphide, because of the lack of an electron donor. Such hypotheses are based on the sulphur isotope composition of native sulphur concretions found in the Lisan Formation. Bishop *et al.* (2013) argue that the absence of pyrite in the sulphate-rich Dead Sea sediment is linked to this incomplete sulphate reduction terminating at S^0, thus allowing mackinawite and greigite, and sometimes pyrite, to coexist, supporting observations from Hunger & Benning (2007) in limiting sulphur conditions.

Changes in limnological regimes results in switches in microbial processes

Microbes in stratified versus mixed water column in the Dead Sea

Microbial life in the Dead Sea is limited by the amount of energy required to equilibrate with a highly

concentrated external medium. As such, metabolic pathways are selected for their efficiency (Oren, 2010). In such a setting, the lake biosphere benefits from freshwater inputs in different ways: (i) a lowering of the salinity of the upper water column, forming a salinity gradient within the lake, (ii) input of normally life limiting nutrients and (iii) creation or input of fresh and labile organic matter (Oren, 1983; Oren *et al.*, 1995).

Periods of lake stratification are thus characterized by an upper layer hosting primary production and a hypolimnion where anaerobic degraders, such as sulphate reducing bacteria or fermenters, can degrade the produced organic matter (Nissenbaum & Kaplan, 1976; Torfstein *et al.*, 2005; Ariztegui *et al.*, 2015). This is reflected by microbial communities in the resulting sedimentary facies (Thomas *et al.*, 2015). On the other hand, during holomictic periods (generally dominant when evaporation largely exceeds precipitation), the absence of water dilution, in conjunction with nutrient starvation and lack of labile organic matter, only allows extreme halophiles such as archaeal members of the *Halobacteria* class to develop and subsist in the water column and in the subsequent sediment (Bodaker *et al.*, 2010; Thomas *et al.*, 2015).

The data presented here agree with such inferences. The presence of framboidal and euhedral pyrite (Fig. 5A and C) in the microbial mat can be explained by the complete sulphate reduction encouraged by the presence of a salinity gradient in the pond and fresh organic material provided by *Dunaliella* algae. Furthermore, it is proposed that pyrite occurs only when enough fresh organic matter is transported to the sediment, with potentially sufficient dilution of the hypolimnion (as suggested by Lazar *et al.*, 2014). Such events could have occurred at the climax of glacial periods in the Dead Sea Basin, for example, during the Lisan period, as observed in the core (Table 1 and Fig. 6). Pyrite could therefore be used as a productivity proxy in the deep Dead Sea sediment. Differential occurrences of iron-sulphur minerals, in particular greigite, in halite and AAD facies also support major variations in the iron, sulphur and carbon cycles in each limnological setting.

Cycling of iron, sulphur and carbon in the dynamic Dead Sea

Examination of changes in major and minor elements in the water column of the Dead Sea during its latest turnover (winter 1978–1979) revealed the impact of lake stratification on the sulphur and iron cycles. Nishri & Stiller (1984) estimated that all dissolved iron in the lake's water column had oxidized within a year after the complete penetration of oxidant waters to the depth of the lake. Iron-sulphur minerals, which used to be observed precipitating directly in those bottom waters, were also fully replaced by iron oxy-hydroxides. Neev & Emery (1967) demonstrated the direct precipitation of iron-sulphur minerals on ropes hanging in the hypolimnion of the Dead Sea before its complete mixing in 1978. Measurement of ferrous iron concentrations in the lake at this time supported a diffusion of dissolved reduced iron from the sediment (Nishri & Stiller, 1984). Analysis of groundwater present in the Dead Sea shore subsurface supports the slow but efficient reduction of iron in the hypersaline subsurface (Kiro *et al.*, 2013). Syngenetic iron-sulphur precipitation is thus possible in the Dead Sea hypolimnion, and probably consumes the available ferrous iron in this water until HS^- or Fe^{2+} is no longer available. The subsequent particulate iron is eventually incorporated within the sediment.

Although available iron reacts with sulphide, shallow sediments only harbour greigite phases, and rarely show pyrite chemistry. Greigite is, for example, seen infilling the chambers of allochtonous foraminifera (Fig. 9) that could originate from ponds around the lake (Almogi-Labin *et al.*, 1992). The organic matter they provide would be readily available for sulphate reducing organisms in the lake. Ferrous iron ions in the water column may allow precipitation of iron sulphides. Iron sulphides within the sediment, however, would enter a zone where fresh organic matter and thus HS^- becomes less available. Similarly, ferrous iron may become less available. Rims of greigite around titano-magnetite (Fig. 8) would support such limitations. Canfield *et al.* (1992) demonstrated that although iron sources are available in the sediment, the reactivity of iron is the key factor in subsurface environments. Potentially, iron oxides form a source of reactive iron in this setting, allowing diagenetic iron sulphide development in the sediment at relatively slow rates. Eventually, growth may continue in the deeper sediment, if enough sulphide accumulates and is allowed to react with iron.

In a fully mixed and halite-precipitating water column, the microbial cycles start only in the shallow sediment, and are relatively slow as no salinity gradient is expected in the deep subsurface. Microbial reduction is thought to be limited and diagenetic transformation occurs at relatively low and steady rates, similar to what could be observed in the deeply buried AAD, but with less labile organic matter available.

Interactions and redox gradients are probably very different from conditions in the shallow parts of the lake. Most information available on the cycling of iron and sulphur in the Dead Sea has been derived from environments where groundwater interacts with the deep brine of the core (Kiro *et al.*, 2013; Avrahamov *et al.*, 2014). The deep sediment experiences almost no interaction with

diluted groundwater and mainly interacts with brine. It is thus likely that the relatively active processes observed in the shores of the Dead Sea, like microbial sulphate reduction, methanogenesis, anaeorobic oxidation of methane and iron reduction and oxidation (Ionescu *et al.*, 2012; Avrahamov *et al.*, 2014), are extremely limited in the deep sediment. Cycles of iron, sulphur and carbon must then be seen very differently in the deeper part of the lake. New work, potentially arising from the study of DSDDP cores, will allow better characterization of the processes at stake in this very peculiar subsurface environment.

Microbial effects on early diagenesis in the deep Dead Sea sediment

Aragonite precipitation in the Dead Sea: abiotic or microbially influenced?

Precipitation of aragonite occurs in the Dead Sea when magnesium/calcium-rich brines of the hypolimnion encounter carbonate-loaded fresher water of the epilimnion. This is thought to occur either through simple addition of these carbonates (Barkan *et al.*, 2001), or through alkalinity rise during CO_2 escape caused by evaporation, or by CO_2 consumption by photosynthetic blooming organisms (Neev & Emery, 1967; Begin *et al.*, 1974; Kolodny *et al.*, 2005). Carbonate ions thus seem to be limiting the precipitation of aragonite in the Dead Sea. As a result, their production in the sediment or at the water sediment interface could be a potential trigger in the precipitation of aragonite, especially since associated metabolic processes promote a rise in alkalinity (Dupraz & Visscher, 2005).

Dupraz *et al.* (2009) have listed potential mechanisms for enhancing calcium carbonate precipitation. Among them, complete sulphate reduction would permit the release of EPS-bound Ca^{2+} as well as carbonate ions by degradation of EPS, raising alkalinity and the $CaCO_3$ saturation index (Visscher *et al.*, 1998, 2000). Effects of sulphate reduction on alkalinity have been lately discussed by Meister (2013) and, in particular, the fact that the production of one H^+ per mole of reduced sulphate also leads to a pH decrease, hence to more carbonate dissolution than precipitation. Such a model seems to be dependent on the type of organic matter used as electron donor (Gallagher *et al.*, 2014).

In the case of the Dead Sea, degradation of EPS and the release of bonded calcium is not required, as suggested in the process of biologically induced mineralization (Dupraz *et al.*, 2009), since calcium is already present in the porewater at extreme concentration. The use of formate or hydrogen as an electron donor for SRB could thus also promote carbonate precipitation in the form of aragonite (Gallagher *et al.*, 2012), and is known to occur at high salinity for various species (Oren, 2010).

The presence of nanospheres in the mat (Fig. 11C), and what seems to resemble the transformation of the organic matrix to calcium carbonate minerals (Fig. 11D), may thus be influenced by the microbial production of carbonate ions in the sediment, from the available allochthonous or autochthonous organic matter. These nanoglobules have been recognized to be the initiating stage of calcium carbonate precipitation in numerous EPS-rich environments (Benzerara *et al.*, 2006; Bontognali *et al.*, 2008; Spadafora *et al.*, 2010), or to be preferentially associated with sulphate reducing bacteria (Aloisi *et al.*, 2006). Eventually, they lead to the formation of stellate aragonite clusters, embedded in, or originating from, the biofilm sheet remains (Fig. 11D–F) as, for example, those observed in the marine stromatolites of Highborne Cay, Bahamas (Reid *et al.*, 2000). The final aragonite morphology is similar to other aragonite precipitates (needles or stellate clusters) in the Dead Sea. Clustering into stars may occur through EPS related nucleation, but also via nucleation on the surface of detrital minerals or bacterial surfaces (Spadafora *et al.*, 2010). No direct morphological characteristic can thus be identified as the only result of the influence of EPS on aragonite precipitation.

While potentially observable in the mat (but not recorded in the bulk aragonite carbon isotopes; unpublished data), microbially influenced aragonite precipitation is unlikely to occur in the core. First of all, no visible proof was identified. An absence of nanoglobules or of conclusive aragonite-EPS interactions and morphologies tends to discriminate against such pathway. Second, this pathway would depend on the complete degradation of organic matter through microbial activity, which is not supported by the data presented here. Instead, this study supports either a slow and/or incomplete sulphate reduction, as previously demonstrated in the Dead Sea environment (Bishop *et al.*, 2013; Häusler *et al.*, 2014), which would have a limited effect on the alkalinity of the sedimentary micro-environment (Dupraz & Visscher, 2005). The impact of calcium carbonate generated via sulphate reduction on the Dead Sea environment should then be minor compared to the huge amount of aragonite needles precipitating in the water column: 15 mol m^{-2} y^{-1} in Lake Lisan (Stein *et al.*, 1997), and 1·4 mol m^{-2} y^{-1} after heavy flooding during winter, 1992 (Barkan *et al.*, 2001). Stable isotopic measurements of bulk aragonitic carbon did not indicate specifically microbially induced fractionation, although some measured values are relatively low (unpublished), suggesting that the impact of such a pathway on the total aragonitic pool is minimal. However, it is relevant in order to better understand future diagenetic

processes affecting porosity and organic matter degradation in hypersaline sediments.

Iron-sulphur minerals as diagenetic imprint of the deep Dead Sea sediment

This study supports diagenetic development of greigite in the deep sediment. This process had already been highlighted by Ron *et al.* (2006) and Frank *et al.* (2007). Iron sulphide rims regularly observed around titano-magnetite in AAD intervals (Figs 7A and 8) suggest rapid reaction of soluble sulphide with dissolved iron originating from the detrital iron fraction. This would undoubtedly affect the magnetic signal of the Dead Sea sediment, as suggested by Rowan & Roberts (2006). Iron-sulphur precipitates have been observed in the halite sections of the core too, when gypsum is an associated evaporative phase (Fig. 10). The detrital component seems to be the source of iron there, and iron-sulphur forms around the gypsum minerals. Different behaviours are thus observed, whether the focus is on sediments derived from arid or more humid periods. This suggests that reduction may also occur in holomictic settings, while it has so far been described mainly from the sediments of Lake Lisan or in general in a stratified lake (Nissenbaum, 1975; Torfstein *et al.*, 2008). This early diagenesis may, however, be erased by a second stage, if sediments are exposed in outcrop and desiccate. For example, neither greigite nor pyrite has been observed in the Masada sections of Lake Lisan (Torfstein *et al.*, 2005; Bishop *et al.*, 2013) and halite intervals dissolve when exposed.

The iron and sulphur cycles are greatly influenced by microbes in the Dead Sea subsurface with phase changes from gypsum sulphate to HS^-, S^0, and iron-sulphur mineralization. The quality of the available organic carbon is critical to the formation of these phases. It also appears that the processes vary depending on whether halite-rich intervals precipitating during arid periods are examined, or AAD intervals characteristic of more humid episodes. Similar to the effects on microbial communities (Ariztegui *et al.*, 2015; Thomas *et al.*, 2015), freshwater inputs largely affect the precipitation and diagenetic processes in the deep Dead Sea Basin.

CONCLUSION

The Dead Sea is a unique system that can hardly be compared to any other hypersaline systems. It possesses some hypersaline biological system characteristics such as specifically adapted microbial communities. However, the latter develop at much slower rates, and with different limiting conditions (low sulphide, high calcium and magnesium concentrations). The drilled record sheds light on the evolution of deep sediments before they undergo dehydration or dissolutive transformation. It implies diagenetic transformations occurring in the deeper part of the basin as follow:

- The formation of iron-sulphur mineralization emphasizes the existence of a microbial sulphur cycle influencing mineral precipitation and organic matter preservation.
- Iron-sulphur minerals are relatively small and often close to greigite in composition, supporting a slow or incomplete microbial sulphate reduction in the Dead Sea sediment, whether arid or more humid conditions prevail. On the other hand, the occurrence of authigenic pyrite may be an important marker of lake productivity.
- The iron cycle is also influenced by secondary dissolution and re-precipitation of magnetic fractions.
- Comparison with an active microbial mat of the Dead Sea shore allowed exopolymeric substances to be detected in the core sediments. Identified mainly based on morphology, they have the potential to serve as templates for aragonite precipitation at depth, implying that aragonite may not only form in the water column under conditions previously envisaged.

Together, these findings support the existence of living microbes in the sediment of the Dead Sea, and remain the only proof for their metabolic activity. Finally, these results have strong implications regarding the fate of organic matter and on processes involved in mineralization and porosity development from the perspective of diagenetic evolution of hypersaline subsurface systems. They also support the microbial impact on the sedimentological and geochemical record of the deep Dead Sea sediment. Such observations must be taken into account in future palaeoenvironmental reconstructions.

ACKNOWLEDGEMENTS

This research was funded by the Swiss National Science Foundation (projects 200021-132529 and 200020-149221/1) for CT and by The Dead Sea Drill Excellence Center of the Israel Science Foundation (grant #1736/11) for YK and YE. This work has been realized in close collaboration with members of the DSDDP Scientific Team, for which a list can be found at www.icdp-online.org. The authors thank the DSDDP technical team in Israel and Potsdam, and the ICDP engineers that have helped in the set-up of the material and the analysis at GFZ Potsdam during core-opening. N. Waldmann and A. Vuillemin are deeply acknowledged for direction and assistance on sampling. P. Dulski and his lab are thanked for XRF core scanning, C. Dupraz, M. Dadras and M. Leboeuf for

Cryo-SEM assistance and advice and J. Garcia-Veigas at the CCiT lab facilities in the University of Barcelona for ESEM. We also thank A. Martignier and R. Martini at the University of Geneva and M. Pacton for their precious SEM expertise. The authors also wish to thank P. Visscher for fruitful conversation and two anonymous reviewers who greatly improved this article. The authors declare no conflict of interest.

References

Abu Ghazleh, S., Hartmann, J., Jansen, N. and **Kempe, S.** (2009) Water input requirements of the rapidly shrinking Dead Sea. *Naturwissenschaften*, **96**, 637–643.

Almogi-Labin, A., Perelis-Grossovicz, L. and **Raab, M.** (1992) Living Ammonia from a hypersaline inland pool, Dead Sea area, Israel. *J. Foraminifer. Res.*, **22**, 257–266.

Aloisi, G., Gloter, A., Kruger, M., Wallmann, K., Guyot, F. and **Zuddas, P.** (2006) Nucleation of calcium carbonate on bacterial nanoglobules. *Geology*, **34**, 1017–1020.

Ariztegui, D., Thomas, C. and **Vuillemin, A.** (2015) Present and future of subsurface biosphere studies in lacustrine sediments through scientific drilling. *Int. J. Earth Sci.*, **104**, 1655–1665.

Astafieva, M.M., Rozanov, A.Y. and **Hoover, R.** (2005) Framboids: their structure and origin. *Paleontol. J.*, **39**, 457.

Avrahamov, N., Yechieli, Y., Lazar, B., Lewenberg, O., Boaretto, E. and **Sivan, O.** (2010) Characterization and dating of saline groundwater in the Dead Sea area. *Radiocarbon*, **52**, 1123–1140.

Avrahamov, N., Antler, G., Yechieli, Y., Gavrieli, I., Joye, S.B., Saxton, M., Turchyn, A.V. and **Sivan, O.** (2014) Anaerobic oxidation of methane by sulfate in hypersaline groundwater of the Dead Sea aquifer. *Geobiology*, **12**, 511–528.

Barkan, E., Luz, B. and **Lazar, B.** (2001) Dynamics of the carbon dioxide system in the Dead Sea. *Geochim. Cosmochim. Acta*, **65**, 355–368.

Begin, Z.B., Ehrlich, A. and **Nathan, Y.** (1974) Lake Lisan: the Pleistocene precursor of the Dead Sea. *Geol. Surv. Isr. Bull.*, **63**, 11–30.

Benzerara, K., Menguy, N., López-García, P., Yoon, T.-H., Kazmierczak, J., Tyliszczak, T., Guyot, F. and **Brown, G.E.** (2006) Nanoscale detection of organic signatures in carbonate microbialites. *Proc. Natl Acad. Sci. USA*, **103**, 9440–9445.

Berner, R.A. (1970) Sedimentary pyrite formation. *Am. J. Sci.*, **268**, 1–23.

Berner, R.A. (1984) Sedimentary pyrite formation: an update. *Geochim. Cosmochim. Acta*, **48**, 605–615.

Bishop, T., Turchyn, A.V. and **Sivan, O.** (2013) Fire and brimstone: the microbially mediated formation of elemental sulfur nodules from an isotope and major element study in the paleo-Dead Sea. *PLoS ONE*, **8**, e75883.

Bodaker, I., Sharon, I., Suzuki, M.T., Feingersch, R., Shmoish, M., Andreishcheva, E., Sogin, M.L., Rosenberg, M., Maguire, M.E., Belkin, S., Oren, A. and **Béjà, O.** (2010) Comparative community genomics in the Dead Sea: an increasingly extreme environment. *ISME J.*, **4**, 399–407.

Bontognali, T.R.R., Vasconcelos, C., Warthmann, R.J., Dupraz, C., Bernasconi, S.M. and **McKenzie, J.A.** (2008) Microbes produce nanobacteria-like structures, avoiding cell entombment. *Geology*, **36**, 663–666.

Bosak, T. and **Newman, D.K.** (2005) Microbial kinetic controls on calcite morphology in supersaturated solutions. *J. Sed. Res.*, **75**, 190.

Braissant, O., Decho, A.W., Dupraz, C., Glunk, C., Przekop, K.M. and **Visscher, P.T.** (2007) Exopolymeric substances of sulfate-reducing bacteria: interactions with calcium at alkaline pH and implication for formation of carbonate minerals. *Geobiology*, **5**, 401–411.

Canfield, D.E., Raiswell, R. and **Bottrell, S.H.** (1992) The reactivity of sedimentary iron minerals toward sulfide. *Am. J. Sci.*, **292**, 659–683.

Defarge, C., Trichet, J., Jaunet, A.M., Robert, M., Tribble, J. and **Sansone, F.J.** (1996) Texture of microbial sediments revealed by cryo-scanning electron microscopy. *J. Sed. Res.*, **66**, 935.

Des Marais, D.J. (1995) The biogeochemistry of hypersaline microbial mats. In: *Advances in Microbial Ecology* (Ed. J.G. Jones), pp. 251–274. Plenum, Springer US, New York.

Drobner, E., Huber, H., Wächtershäuser, G., Rose, D. and **Stetter, K.O.** (1990) Pyrite formation linked with hydrogen evolution under anaerobic conditions. *Nature*, **346**, 742–744.

Dupraz, C. and **Visscher, P.T.** (2005) Microbial lithification in marine stromatolites and hypersaline mats. *Trends Microbiol.*, **13**, 429–438.

Dupraz, C., Visscher, P.T., Baumgartner, L.K. and **Reid, R.P.** (2004) Microbe-mineral interactions: early carbonate precipitation in a hypersaline lake (Eleuthera Island, Bahamas). *Sedimentology*, **51**, 745–765.

Dupraz, C., Reid, R.P., Braissant, O., Decho, A.W., Norman, R.S. and **Visscher, P.T.** (2009) Processes of carbonate precipitation in modern microbial mats. *Earth-Sci. Rev.*, **96**, 141–162.

Frank, U., Nowaczyk, N.R. and **Negendank, J.F.W.** (2007) Palaeomagnetism of greigite bearing sediments from the Dead Sea, Israel. *Geophys. J. Int.*, **168**, 904–920.

Gallagher, K.L., Kading, T.J., Braissant, O., Dupraz, C. and **Visscher, P.T.** (2012) Inside the alkalinity engine: the role of electron donors in the organomineralization potential of sulfate-reducing bacteria. *Geobiology*, **10**, 518–530.

Gallagher, K., Dupraz, C. and **Visscher, P.** (2014) Two opposing effects of sulfate reduction on carbonate precipitation in normal, marine, hypersaline and alkaline environments: COMMENT. *Geology*, **42**, 313–314.

Gavrieli, I., Yechieli, Y., Halicz, L., Spiro, B., Bein, A. and **Efron, D.** (2001) The sulfur system in anoxic subsurface

brines and its implication in brine evolutionary pathways: the Ca-chloride brines in the Dead Sea area. *Earth Planet. Sci. Lett.*, **186**, 199–213.

Glombitza, C., Stockhecke, M., Schubert, C.J., Vetter, A. and **Kallmeyer, J.** (2013) Sulfate reduction controlled by organic matter availability in deep sediment cores from the saline, alkaline Lake Van (Eastern Anatolia, Turkey). *Front. Microbiol.*, **4**, 1–12.

Häusler, S., Weber, M., Siebert, C., Holtappels, M., Noriega-Ortega, B.E., De Beer, D. and **Ionescu, D.** (2014) Sulfate reduction and sulfide oxidation in extremely steep salinity gradients formed by freshwater springs emerging into the Dead Sea. *FEMS Microbiol. Ecol.*, **90**, 956–969.

Hunger, S. and **Benning, L.G.** (2007) Greigite: a true intermediate on the polysulfide pathway to pyrite. *Geochem. Trans.*, **8**, 1.

Ionescu, D., Siebert, C., Polerecky, L., Munwes, Y.Y., Lott, C., Häusler, S., Bižić-Ionescu, M., Quast, C., Peplies, J., Glöckner, F.O., Ramette, A., Rödiger, T., Dittmar, T., Oren, A., Geyer, S., Stärk, H.J., Sauter, M., Licha, T., Laronne, J.B. and **de Beer, D.** (2012) Microbial and chemical characterization of underwater fresh water springs in the Dead Sea. *PLoS ONE*, **7**, e38319.

Kawaguchi, T. and **Decho, A.W.** (2002) Isolation and biochemical characterization of extracellular polymeric secretions (EPS) from modern soft marine stromatolites (Bahamas) and its inhibitory effect on $CaCO_3$ precipitation. *Prep. Biochem. Biotechnol.*, **32**, 51–63.

Kiro, Y., Weinstein, Y., Starinsky, A. and **Yechieli, Y.** (2013) Groundwater ages and reaction rates during seawater circulation in the Dead Sea aquifer. *Geochim. Cosmochim. Acta*, **122**, 17–35.

Kolodny, Y., Stein, M. and **Machlus, M.** (2005) Sea-rain-lake relation in the Last Glacial East Mediterranean revealed by $\delta^{18}O$-$\delta^{13}C$ in Lake Lisan aragonites. *Geochim. Cosmochim. Acta*, **69**, 4045–4060.

Lazar, B., Sivan, O., Yechieli, Y., Levy, E.J., Antler, G., Gavrieli, I. and **Stein, M.** (2014) Long-term freshening of the Dead Sea brine revealed by porewater Cl^- and $\delta^{18}O$ in ICDP Dead Sea deep-drill. *Earth Planet. Sci. Lett.*, **400**, 94–101.

Luther, G.W. (1991) Pyrite synthesis via polysulfide compounds. *Geochim. Cosmochim. Acta*, **55**, 2839–2849.

Meister, P. (2013) Two opposing effects of sulfate reduction on carbonate precipitation in normal marine, hypersaline, and alkaline environments. *Geology*, **41**, 499–502.

Mishra, A. and **Jha, B.** (2009) Isolation and characterization of extracellular polymeric substances from micro-algae Dunaliellasalina under salt stress. *Bioresour. Technol.*, **100**, 3382–3386.

Neev, D. and **Emery, K.** (1967) The Dead Sea, depositional processes and environments of evaporites. *Geol. Surv. Isr. Bull.*, **41**, 147.

Neugebauer, I., Brauer, A., Schwab, M., Waldmann, N., Enzel, Y., Kitagawa, H., Torfstein, A., Frank, U., Dulski, P., Agnon, A., Ariztegui, D., Ben-Avraham, Z., Goldstein, S.L., Stein, M. and **DSDDP Scientific Party** (2014) Lithology of the long sediment record recovered by the ICDP Dead Sea Deep Drilling Project (DSDDP). *Quatern. Sci. Rev.*, **102**, 149–165.

Nishri, A. and **Stiller, M.** (1984) Iron in the Dead Sea. *Earth Planet. Sci. Lett.*, **71**, 405–414.

Nissenbaum, A. (1975) The microbiology and biogeochemistry of the Dead Sea. *Microb. Ecol.*, **2**, 139–161.

Nissenbaum, A. and **Kaplan, I.R.** (1976) Sulfur and carbon isotopic evidence for biogeochemical processes in the Dead Sea. In: *Environmental Biogeochemistry* (Ed. J. Nriagu), pp. 309–325. Ann Arbor Science Publishers, Ann Arbor.

Oren, A. (1983) Population dynamics of halobacteria in the Dead Sea water column. *Limnol. Oceanogr.*, **28**, 1094–1103.

Oren, A. (2001) The bioenergetic basis for the decrease in metabolic diversity at increasing salt concentrations: implications for the functioning of salt lake ecosystems. *Hydrobiologia*, **466**, 61–72.

Oren, A. (2010) Thermodynamic limits to microbial life at high salt concentrations. *Environ. Microbiol.*, **13**, 1908–1923.

Oren, A. and **Gunde-Cimerman, N.** (2012) Fungal Life in the Dead Sea. In: *Progress in Molecular and Subcellular Biology* (Ed. C. Raghukumar), pp. 115–132. Springer, Heidelberg.

Oren, A. and **Shilo, M.** (1982) Population dynamics of Dunaliella parva in the Dead Sea. *Limnol. Oceanogr.*, **27**, 201–211.

Oren, A., Gurevich, P., Anati, D., Barkan, E. and **Luz, B.** (1995) A bloom of Dunaliella parva in the Dead Sea in 1992: biological and biogeochemical aspects. *Hydrobiologia*, **297**, 173–185.

Passier, H., Middelburg, J., de Lange, G.J. and **Böttcher, M.** (1997) Pyrite contents, microtextures, and sulfur isotopes in relation to formation of the youngest eastern Mediterranean sapropel. *Geology*, **25**, 519–522.

Popa, R., Kinkle, B.K. and **Badescu, A.** (2004) Pyrite framboids as biomarkers for iron-sulfur systems. *Geomicrobiol J.*, **21**, 193–206.

Pósfai, M., Buseck, P.R., Bazylinski, D.A. and **Frankel, R.B.** (1998) Reaction sequence of iron sulfide minerals in bacteria and their use as biomarkers. *Science*, **280**, 880–883.

Reid, R.P., Visscher, P.T., Decho, A.W., Stolz, J.F., Bebout, B.M., Dupraz, C., Macintyre, I.G., Paerl, H.W., Pinckney, J.L., Prufert-Bebout, L., Steppe, T.F. and **DesMarais, D.J.** (2000) The role of microbes in accretion, lamination and early lithification of modern marine stromatolites. *Nature*, **406**, 989–992.

Rhodes, M.E., Oren, A. and **House, C.H.** (2012) Dynamics and persistence of Dead Sea microbial populations as shown by high-throughput sequencing of rRNA. *Appl. Environ. Microbiol.*, **78**, 2489–2492.

Rickard, D. (1975) Kinetics and mechanism of pyrite formation at low temperatures. *Am. J. Sci.*, **275**, 636–652.

Rickard, D. and **Luther, G.W.** (1997) Kinetics of pyrite formation by the H_2S oxidation of iron (II) monosulfide in aqueous solutions between 25 and 125°C: the mechanism. *Geochim. Cosmochim. Acta*, **61**, 135–147.

Roesser, M. and **Müller, V.** (2001) Osmoadaptation in bacteria and archaea: common principles and differences. *Environ. Microbiol.*, **3**, 743–754.

Ron, H., Nowaczyk, N.R., Frank, U., Marco, S. and **McWilliams, M.O.** (2006) Magnetic properties of Lake Lisan and Holocene Dead Sea sediments and the fidelity of chemical and detrital remanent magnetization. *New Front. Dead Sea Paleoenviron. Res.*, **Special Pa**, 171–182.

Rowan, C.J. and **Roberts, A.P.** (2006) Magnetite dissolution, diachronous greigite formation, and secondary magnetizations from pyrite oxidation: Unravelling complex magnetizations in Neogene marine sediments from New Zealand. *Earth Planet. Sci. Lett.*, **241**, 119–137.

Schoonen, M.A.A. and **Barnes, H.L.** (1991) Reactions forming pyrite and marcasite from solution: I. Nucleation of FeS_2 below 100 C. *Geochim. Cosmochim. Acta*, **55**, 1495–1504.

Spadafora, A., Perri, E., Mckenzie, J.A. and **Vasconcelos, C.** (2010) Microbial biomineralization processes forming modern Ca: Mg carbonate stromatolites. *Sedimentology*, **57**, 27–40.

Stein, M., Starinsky, I.A., Katz, I.A., Goldstein, J.S.L., Machlus, M. and **Schramm, A.** (1997) Strontium isotopic, chemical, and sedimentological evidence for the evolution of Lake Lisan and the Dead Sea. *Geochim. Cosmochim. Acta*, **61**, 3975–3992.

Steinhorn, I., Assaf, G., Gat, J.R., Nishri, A., Nissenbaum, A., Stiller, M., Beyth, M., Neev, D., Garber, R., Friedman, G.M. and **Weiss, W.** (1979) The Dead Sea: deepening of the mixolimnion signifies the overture to overturn of the water column. *Sci.*, **206**, 55–57.

Sweeney, R.E. and **Kaplan, I.R.** (1973) Pyrite Framboid Formation; Laboratory Synthesis and Marine Sediments. *Econ. Geol.*, **68**, 618–634.

Tahal Group and the Geological Survey of Israel (2011). Red Sea to Dead Sea Water Conveyance (RSDSC) Study Program: Dead Sea Study.

Thomas, C., Ionescu, D., Ariztegui, D. and the DSDDP Scientific Party (2014) Archaeal populations in two distinct sedimentary facies of the subsurface of the Dead Sea. *Mar. Genomics*, **17**, 53–62.

Thomas, C., Ionescu, D., Ariztegui, D. and the DSDDP Scientific Team (2015) Impact of paleoclimate on the distribution of microbial communities in the subsurface sediment of the Dead Sea. *Geobiology*, **13**, 546–561.

Torfstein, A., Gavrieli, I. and **Stein, M.** (2005) The sources and evolution of sulfur in the hypersaline Lake Lisan (paleo-Dead Sea). *Earth Planet. Sci. Lett.*, **236**, 61–77.

Torfstein, A., Gavrieli, I., Katz, A., Kolodny, Y. and **Stein, M.** (2008) Gypsum as a monitor of the paleo-limnological–hydrological conditions in Lake Lisan and the Dead Sea. *Geochim. Cosmochim. Acta*, **72**, 2491–2509.

Torfstein, A., Goldstein, S.L., Kushnir, Y., Enzel, Y., Haug, G. and **Stein, M.** (2015) Dead Sea drawdown and monsoonal impacts in the Levant during the last interglacial. *Earth Planet. Sci. Lett.*, **412**, 235–244.

Visscher, P.T., Reid, R.P., Bebout, B.M., Hoeft, S.E., Macintyre, L.G. and **Thompson, J.A.** (1998) Formation of lithified micritic laminae in modem marine stromatolites (Bahamas): the role of sulfur cycling. *Am. Mineral.*, **83**, 1482–1493.

Visscher, P.T., Reid, R.P. and **Bebout, B.M.** (2000) Microscale observations of sulfate reduction: correlation of microbial activity with lithified micritic laminae in modern marine stromatolites. *Geology*, **28**, 919–922.

Vuillemin, A., Ariztegui, D., Coninck, A., Lücke, A., Mayr, C. and **Schubert, C.** (2013) Origin and significance of diagenetic concretions in sediments of Laguna Potrok Aike, southern Argentina. *J. Paleolimnol.*, **50**, 275–291.

Wang, Q. and **Morse, J.W.** (1996) Pyrite formation under conditions approximating those in anoxic sediments I. Pathway and morphology. *Mar. Chem.*, **52**, 99–121.

Wilkin, R.T. and **Arthur, M.A.** (2001) Variations in pyrite texture, sulfur isotope composition, and iron systematics in the Black Sea: evidence for Late Pleistocene to Holocene excursions of the O_2–H_2S redox transition. *Geochim. Cosmochim. Acta*, **65**, 1399–1416.

Wilkin, R.T. and **Barnes, H.L.** (1996) Pyrite formation by reactions of iron monosulfides with dissolved inorganic and organic sulfur species. *Geochim. Cosmochim. Acta*, **60**, 4167–4179.

Wilkin, R.T. and **Barnes, H.L.** (1997) Formation processes of framboidal pyrite. *Geochim. Cosmochim. Acta*, **61**, 323–339.

Supporting Information

Additional Supporting Information may be found online in the supporting information tab for this article:

Figure S1. Scanning electron microscope photograph of an aragonite needle of the microbial mat embedded in EPS after cryo-dehydration. EDS measurements 1 presents an enrichment in Chlorine (Cl), Magnesium (Mg) and Calcium (Cl) that could result in the loading of these ions onto the EPS. As a comparison, measurement 2 taken on the aragonite needle is mainly composed of CaCO3. Peaks of Mg and Cl could be related to the EPS composition. They could also be part of other mineral phases underneath the EPS and aragonite needle, which are not visible here.

